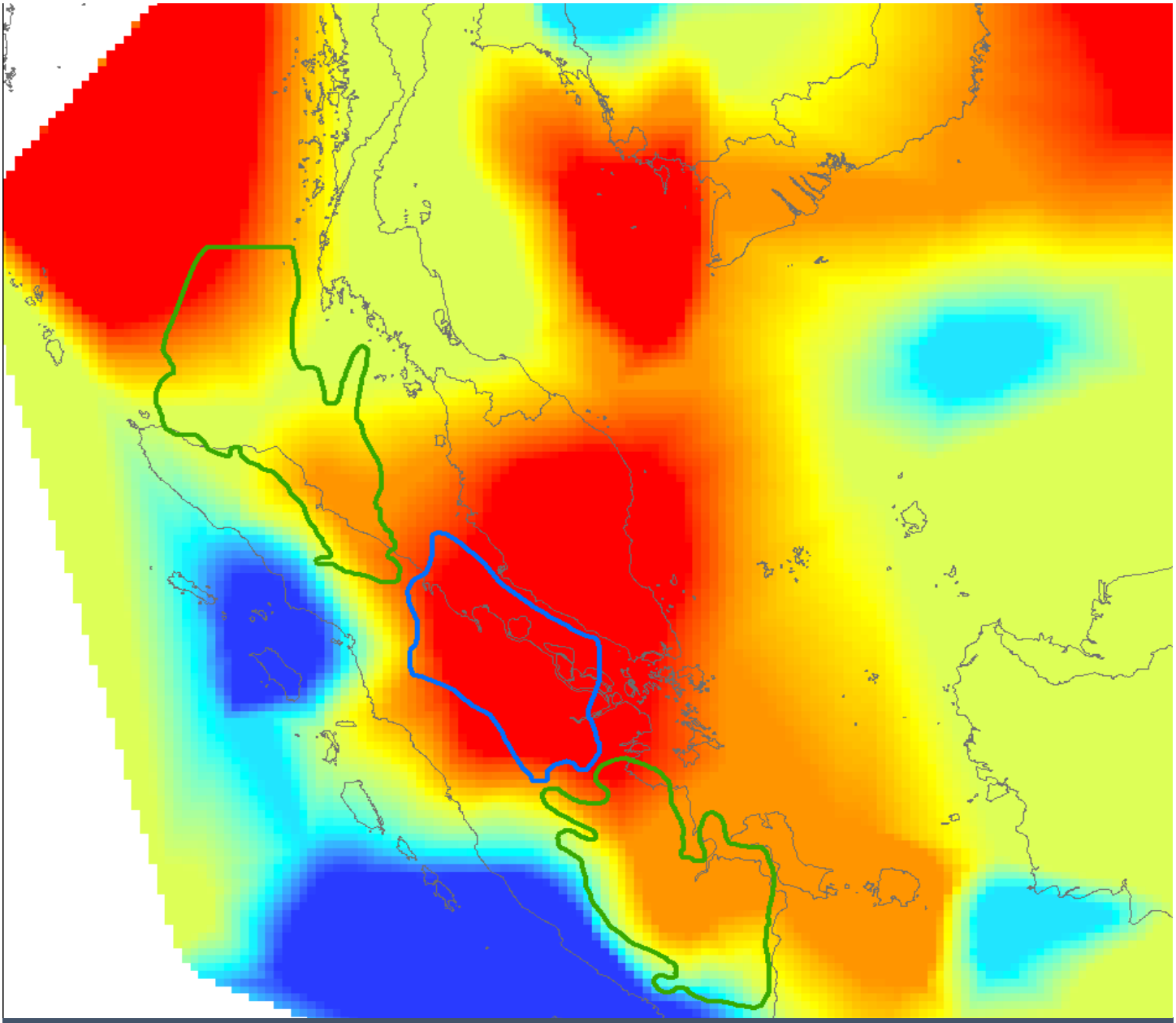

Lithospheric-scale thermal characterization of Central Sumatra Basin, Indonesia

Master Thesis Report

7/13/19

GEO4-1520 MSc Research

Utrecht University

Lithospheric-scale thermal characterization of Central Sumatra Basin, Indonesia

Master Thesis Report

August 6th, 2019

Ikbal Alamsyah Apendi

6204236

Supervised by:

dr. Damien Bonté

Lukman Sutrisno

Department of Earth Sciences

Utrecht University

Abstract

Sumatra, the world's sixth-largest island, is located in the western part of Indonesia. It extends across the equator for 1760 km with an NW-SE orientation. The Central Sumatra Basin is one of the 3 back-arc basins on the northeastern side of the island. The subsurface temperature distribution of the Central Sumatra Basin is estimated with the primary objective to get a better understanding of the thermal characterization and the presence of a high-temperature anomaly in the area. Two research steps were taken to answer these questions, including the 3D geological modeling and temperature modeling. The first step involves the 3D geological modeling of the area. The modeling is based on the geological information from 185 exploration wells and uses the geospatial interpolation method. The results are presented as five top structure maps for each sedimentary unit, including the Minas, Petani, Telisa, Sihapas, and Pematang Group, and one map for the basement. The second step involves the 3D temperature modeling using a thermal-tectonic forward modeling method, constraining the subsurface temperature measurements in the Central Sumatra Basin. The temperature measurements consist of 122 temperature data in total, including 118 uncorrected BHTs and 4 DSTs. The AAPG statistical method was used for the correction of the BHT and resulted in a set of 118 corrected BHTs with better reliability. From this whole dataset, the average thermal gradient is 52.2^{o}C/km, with a surface temperature of 29^{o}C. From the 3D temperature models, the best thermal model corresponds to the lithospheric thickness of 90 km and an old (>500 Ma) upper crust of granitic composition, with relatively high radiogenic heat production. Both the relatively thin lithosphere and the enhanced heat production contributes to the high-temperature anomaly in the area. The increased upper crust heat production might have been caused by the partial melting and crustal reworking due to major tectonic events such as block separation from the East Gondwana, crustal accretion of the Sibumasu and Cathaysia block, and Sumatran orogenesis within the extended time range of Pre-Devonian to Early Tertiary. The pattern distribution of temperature anomalies in the area is also affected by the basin structure of the Central Sumatra Basin.

Keywords: Geological modeling, temperature modeling, high-temperature anomaly, Central Sumatra Basin, Sumatra, Indonesia

Contents

List of Figures

List of Tables

Lithospheric-scale thermal characterization of Central Sumatra Basin, Indonesia

1. Introduction

1.1 Background

Geothermal energy has been one of the most important alternatives for energy source with considerable potential for growth in country with active volcanism such as Indonesia. Not only does it provide the alternative energy, but it also contributes to reducing the effects of global warming and public health risks due to the use of conventional energy sources, as well as our dependence on fossil fuels. Geothermal resources can be classified as low, medium, and high enthalpy, and the uses of geothermal resources will depend on this classification. For example, the geothermal use for electricity generation will require higher enthalpy than for district heating. According to the World Energy Council, the global geothermal installed capacity has reached 83.4 GW, with Indonesia as one of the countries with the largest installed capacity, along with the US, Philippines, Mexico, and New Zealand. Indonesia is the second producer of electricity from geothermal with an installed capacity of 1925 MW (May 2018).

Sumatra, the world's sixth-largest island, is located in the western part of Indonesia. It extends across the equator for 1760 km with an NW-SE orientation. Sumatra island is located in the southeastern part of the Eurasian plate and is the southwestern margin of the Sundaland (Barber, et al., 2005). The island is a part of the subduction system between Indo-Australian and Eurasian Plates, which results in a volcanic arc along the western side of the island, as a part of 'Ring of Fire' (Heidrick & Aulia, 1993). The subduction is also responsible for the formation of three back-arc basins in Sumatra, namely North, Central, and South Sumatra Basin. The Central Sumatra Basin is an active back-arc basin, located on the eastern side of Sumatra (De Coster, 1974), and is in the central position as part of three Sumatran back-arc basins. The basin is a hydrocarbon-rich, Tertiary basin in Indonesia (Heidrick & Aulia, 1993).

The focus of this study will be on the Central Sumatra Basin (De Coster, 1974) as it shows a compelling feature for the development of low to medium enthalpy geothermal. Various temperature studies reported the presence of significantly high heat flow in the region, which extends from Sumatra to Malaysia and as far as Borneo (Carvalho, et al., 1980; Hall, 2002; Grysen, et al., 2016). The Central Sumatra Basin, as a part of this vast region with temperature anomaly, has the highest values. The calculated heat flow for the basin ranges from $77\ mW.m^{-2}$ to $369\ mW.m^{-2}$, corresponding to the geothermal gradient values of $35°C/km$ to $191°C/km$ (Grysen, et al., 2016)

Consequently, Sumatra, especially the Central Sumatra Basin, might have a huge potential for geothermal utilization. The Central Sumatra Basin is a hydrocarbon-rich Tertiary basin (Heidrick & Aulia, 1993), with sufficient information about the subsurface that could help us define the structure and composition of the basin from the preexisting dataset. The presence of porous and permeable reservoir rock units and remarkably high heat flow in the basin make the potential for geothermal utilization in the Central Sumatra Basin. To help with the development of thepotential resource, we have started this work to definie more precisely the resource and its location.

This study will aim to build the lithospheric-scale thermal structure of the Central Sumatra Basin, focusing on the top few kilometers. The main objective of the research is to get a better understanding of the thermal structure of the Central Sumatra Basin, which is now still poorly understood. This study

will address the influence of the geology, heterogeneity, lithospheric-, and tectonic settings of the Central Sumatra Basin on its thermal structure.

1.2 Previous works on the temperature in the Central Sumatra Basin

The research regarding the temperature model in the Central Sumatra Basin is still poorly constrained. The first and only published paper reference to temperature research in the Central Sumatra Basin is from Carvalho et al. (1980) (Figure 1). The research provided a heat flow map of the area using the interpolation method, and it is reported that the average of the heat flow in the area of the basin is around $136.9\ mW.m^{-2}$, which is about twice the world's average. This reference also addressed the possible deep-rooted anomaly occurred in the area of the Central Sumatra Basin.

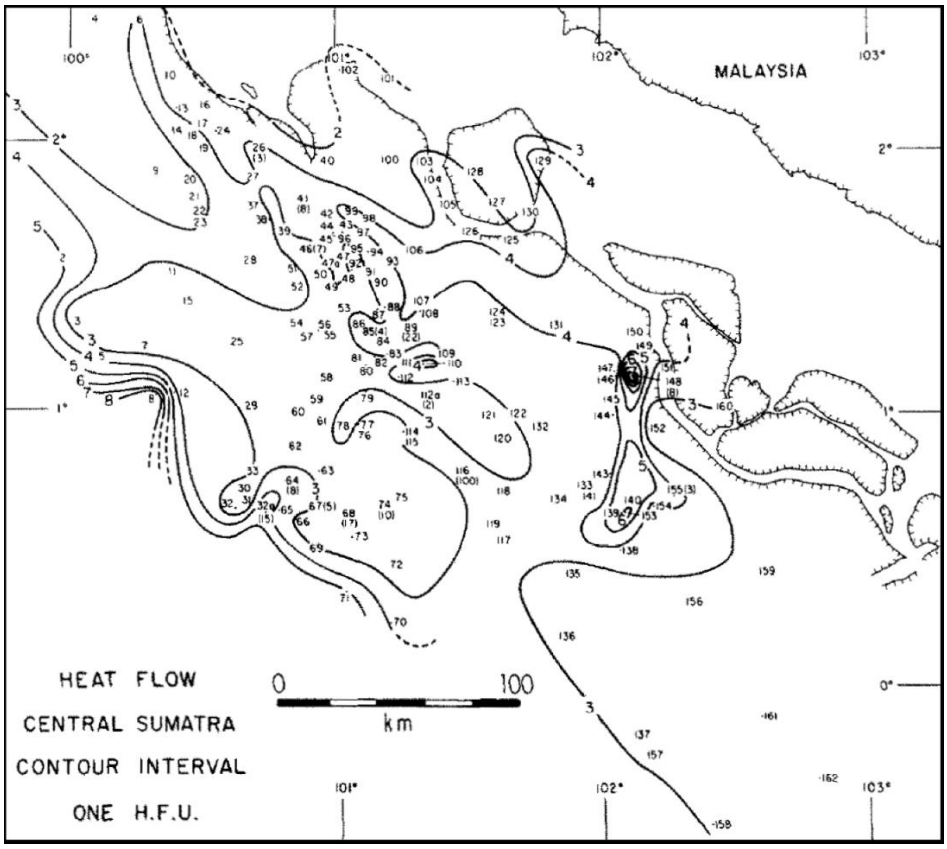

Figure 1. Heat flow map of the Central Sumatra Basin contoured with an interval of 1 HFU (Heat Flow Unit) = 10^{-6} cal.cm^{-2}.sec^{-1} = 41.87 mW.m^{-2} (Carvalho, et al., 1980). (The numbers distributed on the map show the ID of the well used by the reference for generating the map)

The second reference came from a poster of Hall (2002) (Figure 2), which provided a regional heat flow map of Southeast Asia. The map shows the presence of significantly high heat flow in a vast area, which extends from the eastern part of Malayan Peninsular to Sumatra, including the Central Sumatra Basin, and as far as Borneo. Hall (2002) also provided a compilation of temperature dataset for the Southeast Asia region that was used for generating the heat flow map.

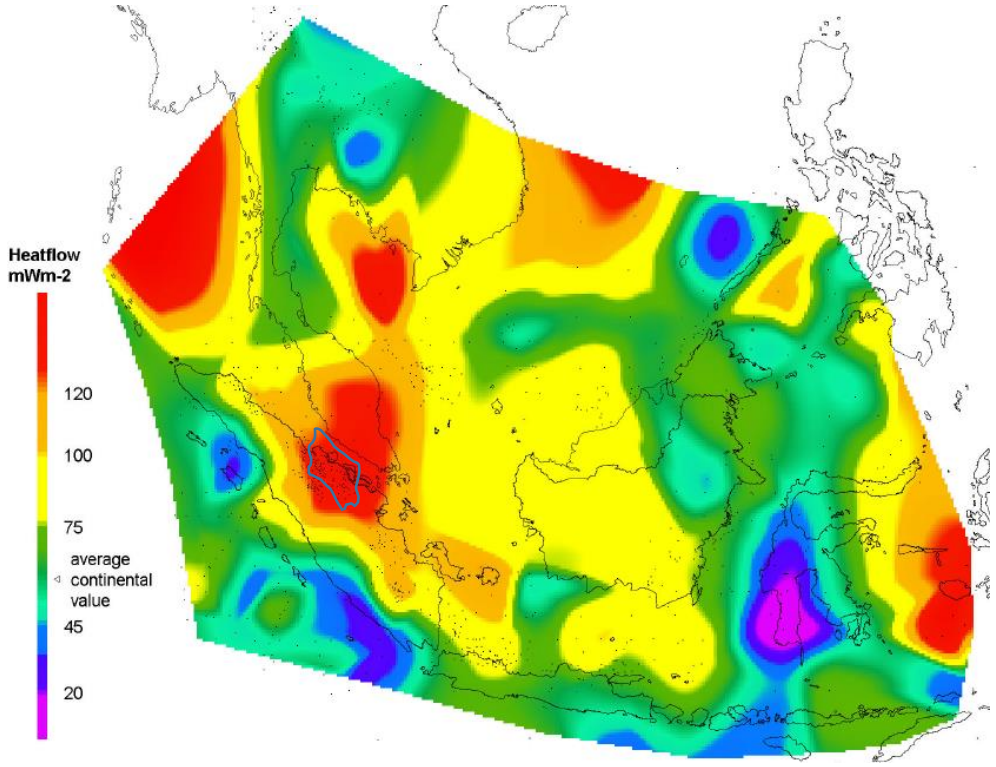

Figure 2. Heat flow map of Southeast Asia, showing a significantly high heat flow anomaly (red area) in the Central Sumatra Basin (blue outline) (Hall, 2002)

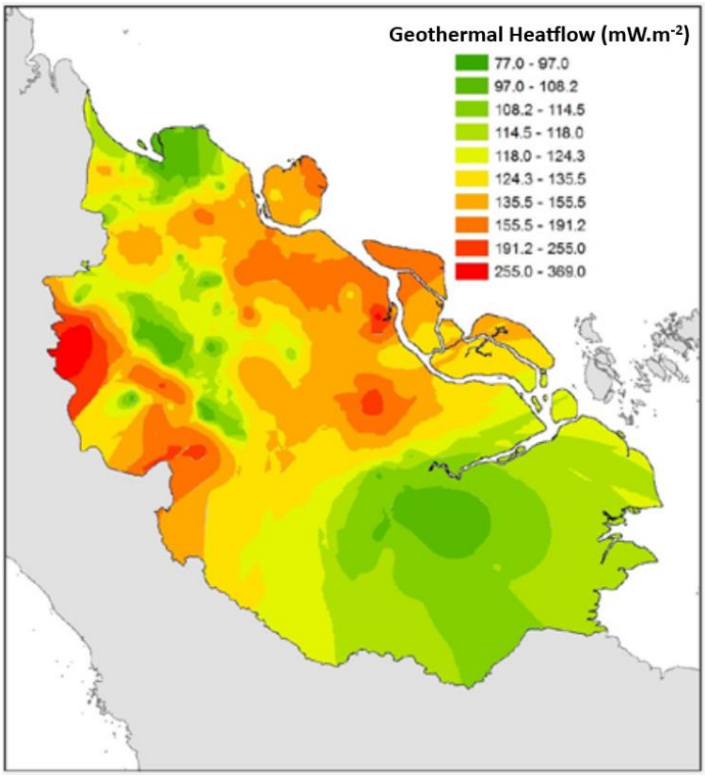

Figure 3. Heat flow map of the Central Sumatra Basin (Grysen, et al., 2016)

The most recent work about the temperature in the Central Sumatra Basin also comes from another published poster from Grysen et al. (2016) (Figure 3). This reference provided both heat flow map and geothermal gradient map of the Central Sumatra Basin, generated from borehole temperature data from hundreds of well. The result reported that the calculated heat flow for the basin ranges from 77 $mW.m^{-2}$ to 369 $mW.m^{-2}$, corresponding to the geothermal gradient values of 35°C/km to 191°C/km.

2. Basin structure and tectonic setting

Understanding the basin structure and the tectonic setting of the area is very important as they can strongly affect the temperature distribution, in addition to the thermal properties. Therefore, the outline of the tectonic evolution, as well as the regional geological history of the major structural elements in Sumatra, including the Central Sumatra Basin, and the associated stratigraphic units, will be described here.

The Central Sumatra Basin, and Sumatra as a whole, is a part of Sundaland (also known as the Sunda Plate), which comprises the southeastern part of the Eurasian Plate. Sumatra is an active southwestern margin of the Sundaland, where a chain of active volcanoes, as a part of 'Ring of Fire,' occurs due to the subduction between Indo-Australian and Eurasian Plates. Sumatra was established by the accretion of several continental and oceanic microplates through time. The outline of the tectonic setting of Sumatra will be mainly focused on two time-periods, which are the period of 'Pre-Tertiary' (Figure 4) and 'the Tertiary to present' (Figure 5). The tectonic evolution of Sumatra and Sundaland as a whole will be discussed in the 'Pre-Tertiary' section, to address the basement of the basin, while the basin structure of the Central Sumatra Basin, as well as the associated stratigraphic units (Figure 7), will be mainly discussed in the 'Tertiary to present' section.

2.1 Pre-Tertiary

During Devonian, the continental blocks of North China, South China, and Indochina, often referred to as Cathaysia, were separated from the northern margin of the East Gondwana (Figure 4a and Figure 4b) (Metcalfe, 1996). These continental blocks were separated through the development of the Paleo-Tethys (Figure 4b) (Barber, et al., 2005). The West Sumatra and East Malaya Block were parts of the Indochina Block of Cathaysia, with West Sumatra Block being its southern margin, separating the block from the Paleo-Tethys ocean (Barber, et al., 2005).

Following the Cathaysia Block separation, the Sibumasu Block, which consists of West Malaya and East Sumatra Block, were also separated in the Late Carboniferous from the northern margin of East Gondwana, or more specifically, from the present-day northwestern margin of Australia (Figure 4c) (Barber, et al., 2005). The rifting of the Sibumasu Block resulted in the development of Meso-Tethys ocean (Figure 4c) (Barber, et al., 2005).

In Early Permian, Paleo-Tethys, which separated the Cathaysia and Sibumasu Block, subducted below the western and southern margin of the Cathaysia Block, and consequently resulted in magmatism such as granite and other types volcanic rock in East Malaya and West Sumatra Block as the western and southern margin of the Cathaysia Block respectively (Barber, et al., 2005). In Middle Permian, the Sibumasu Block moved towards the north through the expansion of Meso-Tethys ocean, which eventually led to the closing of Paleo-Tethys and furthermore the convergence of Cathaysia and Sibumasu Blocks (Figure 4d) (Barber, et al., 2005). By Late Permian, the Paleo-Tethys was completely subducted and consequently resulted in the collision between the Cathaysia and Sibumasu Blocks (Barber, et al., 2005). The collision was responsible for the creation of the Bentong-Raub Suture and Bangka accretionary complex as a margin, separating East and West Malaya, as a part of Cathaysia and Sibumasu Block respectively (Figure 4d) (Barber, et al., 2005).

In Early Triassic, the expansion of the Meso-Tethys eventually led to the translation of West Sumatra Block along the western and southern margin of Sibumasu Block through a major strike-slip fault (Figure

4e), which is now recognized as a Medial Sumatra Tectonic Zone (MSTZ), separating the West Sumatra Block from the East Sumatra of the Sibumasu Block (Barber, et al., 2005). From this period forward, the Sibumasu Block, together with the Indochina and West Sumatra Block of Cathaysia, established the Sundaland.

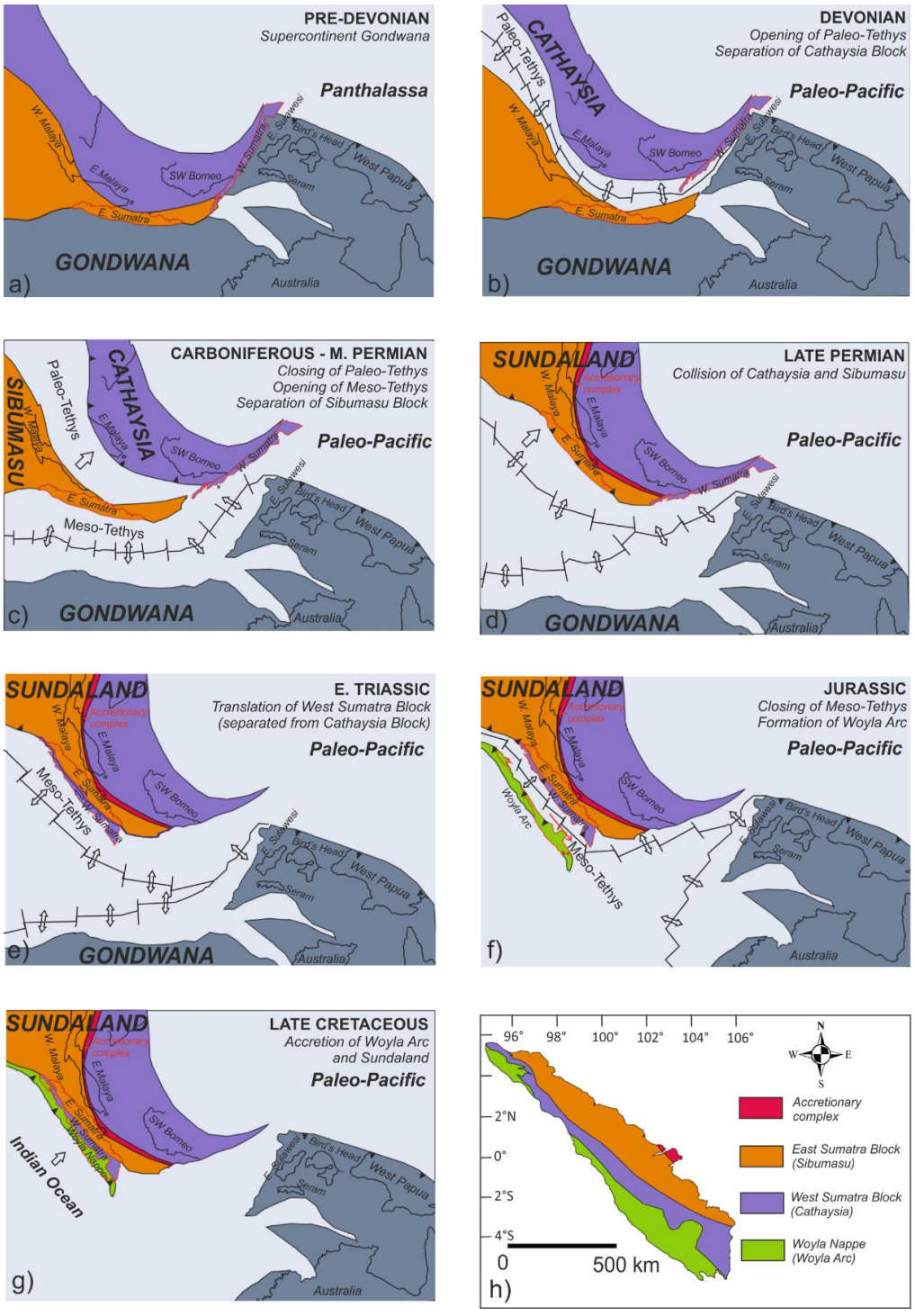

Figure 4. Paleogeographic maps of Southeast Asia showing the tectonic evolution of Sumatra and the surrounding area (a to g) and a map of the pre-Tertiary tectonic block of Sumatra (after Barber et al., 2005)

During the Middle to Late Triassic, a NE-SW regional extension occurred in Sumatra and the Malaya Peninsular, and resulted in the N-S and NW-SE graben and horst structures, where the deep-sea sediments such as cherts and thin shales were deposited in the grabens, and the horsts was dominated by carbonate reef (Barber, et al., 2005).

Following the establishment of Sundaland, the Meso-Tethys subducted in the eastward direction towards the West Sumatra Block as the margin of the Sundaland in Early Cretaceous, resulted in the magmatic arc in the West Sumatra (Barber, et al., 2005). In Late Cretaceous, due to the obliquity of the transform faults and different rate of Meso-Tethys spreading in different blocks, a segment of Meso-Tethys also subducted to another segment of its own in the westward, resulted in the formation of oceanic arc, called Woyla Arc (Figure 4f) (Barber, et al., 2005). The Woyla Arc, separated a segment of Meso-Tethys with the Triassic deep-sea sediments on the grabens and the carbonate reefs on the horsts, from the rest of the Meso-Tethys. The subductions of this segment in both east and west directions eventually led to the closing of this particular Meso-Tethys segment, and the convergence of Woyla Arc and the Sundaland (Figure 4g).

By Late Cretaceous, the Meso-Tethys segment was completely subducted below the Sundaland and the Woyla Arc (Figure 4g) (Barber, et al., 2005). This event resulted in the convergence of both blocks, the formation of accreted Woyla Terrain, and also the renewed subduction of the present-day Indo-Australian ocean plate (or Indian ocean plate) (Barber et al., 2005). The Woyla Terrain consists of Woyla Nappe, where the oceanic island arc from the Woyla Arc being overthrusted onto the Sundaland margin, and the Late Cretaceous magmatic arc of the future Barisan Mountain from the renewed subduction. The area that was intruded by this magmatic arc became a massive shear zone and resulted in the transcurrent fault, which would eventually become the present-day Sumatran Fault (Barber, et al., 2005).

From the Late Cretaceous to Early Paleogene, the distal part of Woyla Nappe was uplifted and exposed the whole complex basement of Sumatra (Figure 4h) (Barber, et al., 2005). The Pre-Tertiary tectonic setting of the Sumatra, highlights the basement of Sumatra as a complex mixture of different lithologies, such as igneous and volcanic rocks due to the magmatism, various sedimentary rocks, for example, the deep-sea deposits and the carbonates at the accretionary wedge, and lastly the various metamorphic rocks resulted by convergence and subduction events.

2.2 Tertiary to present

The structure of the Central Sumatra Basin and the associated stratigraphic units (Figure 7) are mainly defined from Tertiary to present. Throughout the Late Cretaceous to Early Paleogene, the pre-tertiary basement of Sundaland, including Sumatra, extended as far as the present fore-arc islands, and it was exposed to erosion (Barber, et al., 2005).

During the Early Paleogene, the area is considered to have undergone the final stage of stable craton of Sundaland, or pre-rift phase (Figure 5), not at least until the later extension phase in Late Eocene (Barber, et al., 2005). There is barely any stratigraphic unit that is well-recorded in the most area of Sumatran back-arc basins to explain this pre-rift phase, at least not until the Late Eocene, which might indicate that the area was stable until a change in regional tectonic regime in Late Eocene (Barber, et al., 2005).

In the Late Eocene and Early Oligocene, a regional extension occurred throughout much of Southeast Asia. This event coincided with the collision of India with the southern margin of the Asian continental

plate (Barber, et al., 2005), and it has been associated to the extrusion and rotation of the Sundaland Block to the southeast side of the collision site (Tapponier, et al., 1982). This extension resulted in the formation of horsts and grabens that controlled the stratigraphic development at that period (Figure 5).

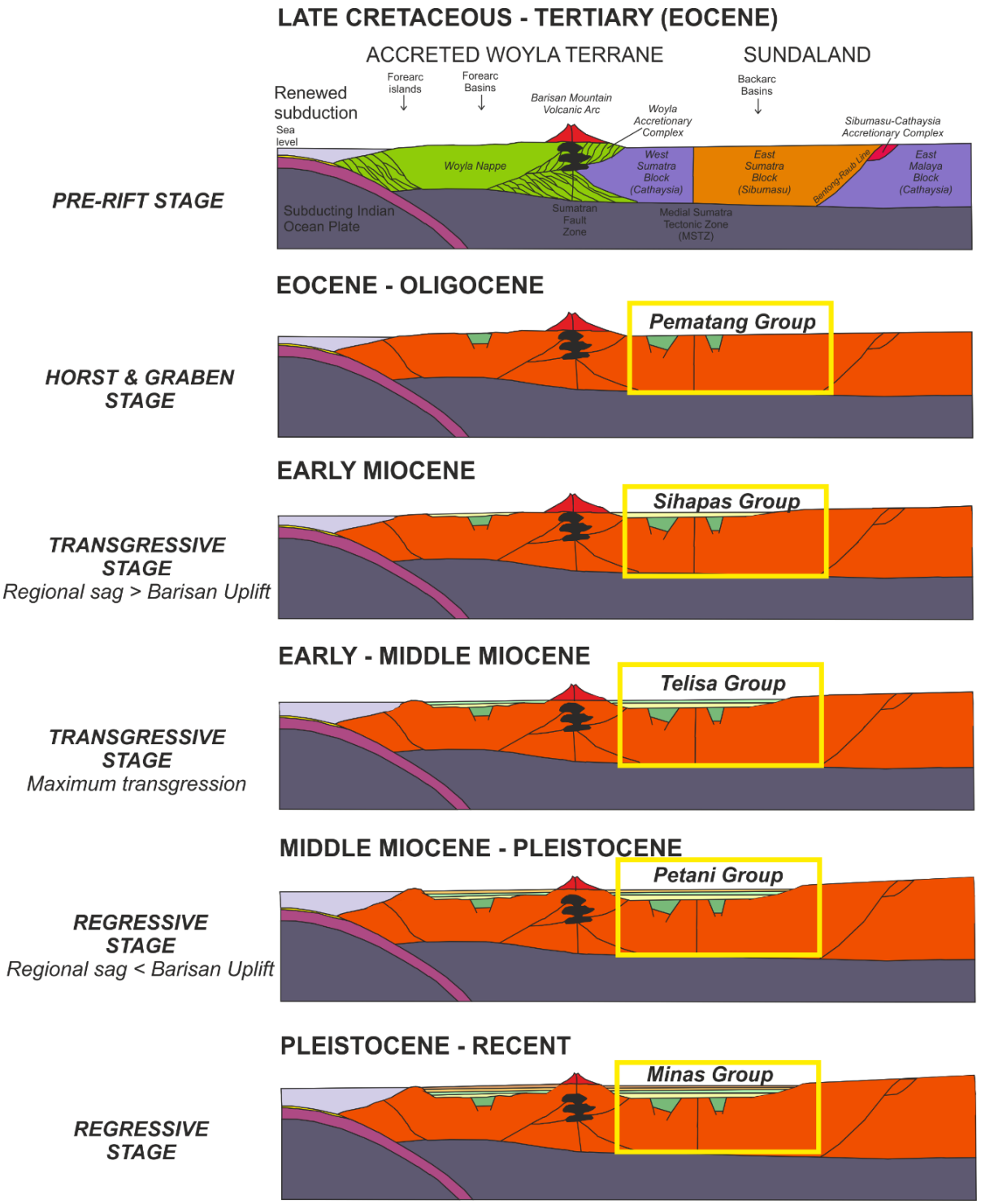

Figure 5. Schematic cross-section of the Sumatra, showing the tectonic evolution of Sumatra from Tertiary to present, including the Central Sumatra Basin (yellow square area) (after Barber et al., 2005)

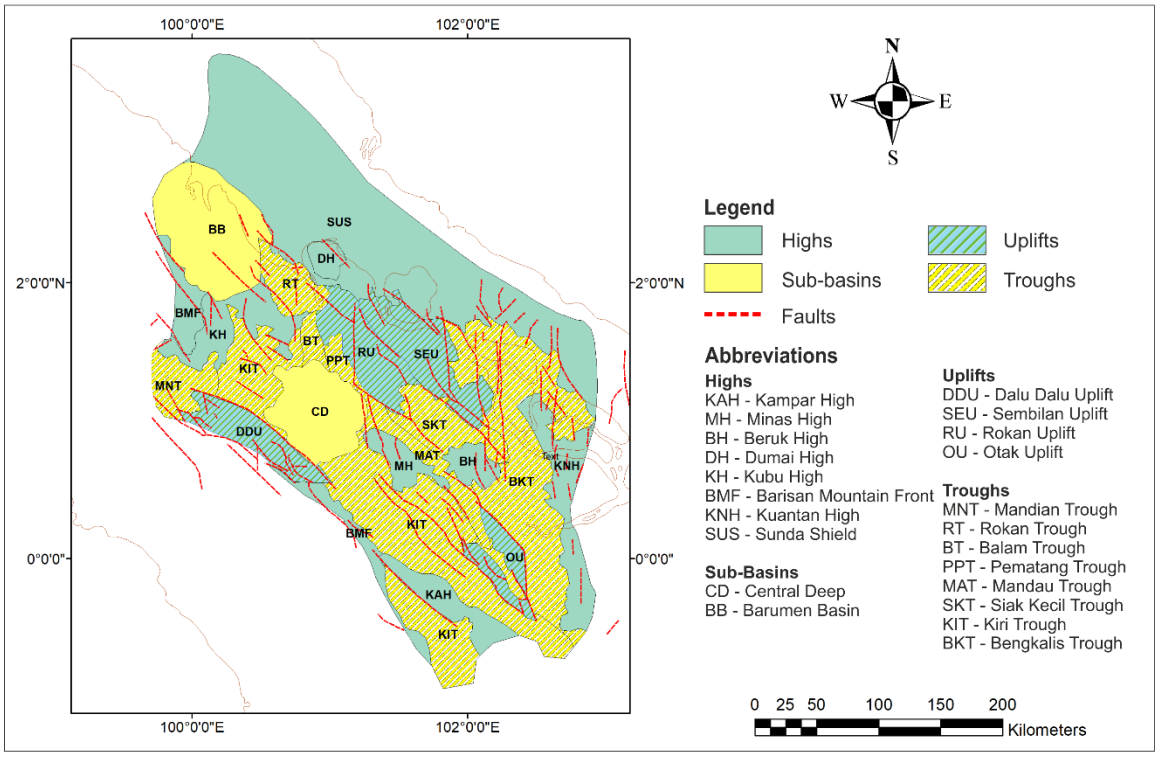

Figure 6. Map of the structural elements of the Central Sumatra Basin (after Barber et al., 2005)

During the Horst and Graben stage, the deposition in much of the Sumatra region was characterized by the sediment that was transported over short distances (Barber, et al., 2005). At this time, the subsidence rate in the grabens was faster than the sedimentation rate, which resulted in the thick accumulation of organic-rich lacustrine deposit, with sedimentologically immature sediments being deposited along the lake shoreline (Barber, et al., 2005). Although the development of grabens in this period is older than the development of the present-day back-arc basins, the sedimentary deposits from this stage is still recognizable in localized stratigraphic nomenclature of the present basins in Sumatra and they play a vital role in their petroleum geology as a significant source rock (Barber, et al., 2005)). In the Central Sumatra Basin, this deposit is recognized as Pematang Group, which is unconformably deposited above the basement. This stratigraphic unit consists of a variety of red, green, and black conglomerates and breccia, with fine- to medium- sandstone claystone, and shales (Barber, et al., 2005). These deposits are interpreted as continental deposits of scree, alluvial fan, fluvial, and lacustrine, with the local euxinic condition and a minor marine influence (Barber, et al., 2005). The euxinic shale, which is part of the Pematang Brown Shale formation, plays a significant role as the source rock in the Central Sumatra Basin (Barber, et al., 2005). Following the deposition of the rift sediment in Horst and Graben stage, a change in the regional tectonic regime occurred in the Late Oligocene, where the uplifted area, represented by Barisan Mountain, became contrasted with other areas of continued sedimentation in the back-arc and fore-arc basins. This event resulted in the local inversions and subsequently led to the regional unconformity between the rift deposit and the later deposits (Barber, et al., 2005).

Following the tectonic regime change in the Late Oligocene, the transgressive stage started occurring in the area, which was caused by the regional sag (Figure 5) (Barber, et al., 2005). The early transgressive stage occurred in Early Miocene, and it marks the first differentiation between the Barisan Mountains and the fore-arc and back-arc basins, thus makes the Barisan Mountain as an important source of sedimentation for the basins (Barber, et al., 2005). Initially, the rate of subsidence was more prominent in the back-arc areas than any other areas but still did not outpace the rate of sedimentation. As a result, the sediments were transported over long distances in the back-arc areas and extended well beyond the pre-existed rift margins through the interconnected fluvial and deltaic system (Barber, et al., 2005). In the Central Sumatra Basin, these early transgressive phases are represented as the lower part of Sihapas Group, which includes Lower Sihapas and Menggala Formation of (Barber, et al., 2005). These stratigraphic units are defined as fine- to coarse- sandstones with pebble conglomerates, local tuffaceous, coal seams, and minor fluvio-deltaic shales (Mertosono & Nayoan, 1974).

In the late Early Miocene to Mid-Miocene, the uplift of Barisan Mountain is slower than the regional sag (Figure 5) (Barber, et al., 2005). As a result, the subsidence rate outpaced the sedimentation rate and resulted in the depositional change from fluvial and deltaic system to open marine system (Barber, et al., 2005). In the Central Sumatra Basin, this event is still recognizable in the stratigraphic nomenclature as the upper part of Sihapas Group, which consists of Upper Sihapas and Duri Formation, and Telisa Formation. The upper part of Sihapas is interpreted as fluvio-deltaic sandstone that came from the Malaysian Shield, deposited in the deltaic and braided river system, while the Telisa Formation is composed of marine shales (Barber, et al., 2005). The maximum transgression stage in Sumatra occurred in Mid-Miocene (Figure 5), and it is indicated by the minimum clastic influx and the maximum marine shale deposition (Barber, et al., 2005). In the Central Sumatra Basin, the maximum transgression is recognizable as a vast marine shale deposition of the upper part of Telisa Formation (Barber, et al., 2005).

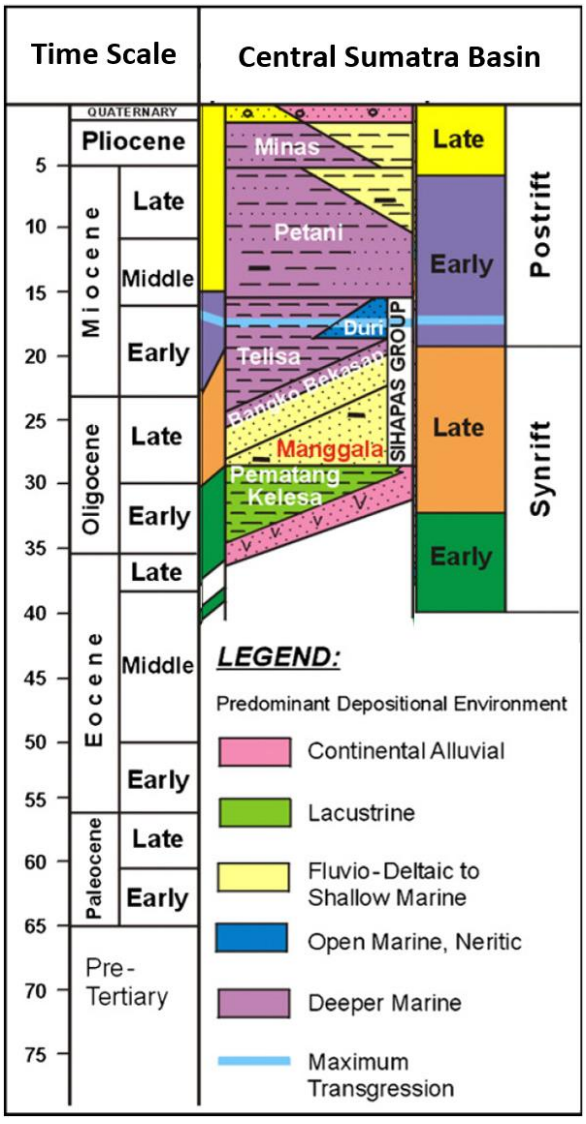

Figure 7. Regional stratigraphic column of the Central Sumatra Basin (Doust & Noble, 2008)

From mid-Miocene onwards, the continuing regional sag started becoming slower than the uplift of the Barisan Mountain and caused a regressive stage (Figure 5) (Barber, et al., 2005). At this time, the fore-arc and back-arc basins continued to subside, while the Barisan Mountains continued to emerge and became a significant sediment source. (Barber, et al., 2005). This event coincided with the activity of the Sumatran Fault System in the Miocene and continued transpressional and trans-tensional movement along the fault until the present day (Barber, et al., 2005). In Late Miocene onwards, turbiditic sandstone

increased, as represented in Lower Petani Formation in the Central Sumatra Basin (De Coster, 1974). By Late Miocene and Early Pliocene, the deposits had gradually changed into shallow marine, sublittoral, and deltaic sediments, which are recognized as Upper Petani Formation in the Central Sumatra Basin (De Coster, 1974). By Late Pliocene, the sediments deposited were dominated by terrestrial sands and clay, and they are recognized as Minas Formation (Cameron, et al., 1981). In Late Pliocene, the uplift and erosion of the Barisan Mountains reached a climax phase, accompanied by intense volcanism (Barber, et al., 2005). This event also coincided with the inversion tectonics that occurred in the back-arc area and associated with the displacement along the Sumatran Strike-Slip Fault (Eubank & Makki, 1981). The Quaternary deposits were unconformably deposited above the eroded surfaces of the structures from the last inversion tectonics (Barber, et al., 2005). These Quaternary deposits consist of coarse conglomerates with volcanic debris from Barisan in the areas that are adjacent to the mountains, fluvial deposits away from the mountains, swamp deposit to the east along the coastline, and deep-sea clays and turbidites in the offshore area (Barber, et al., 2005).

3. Methodology

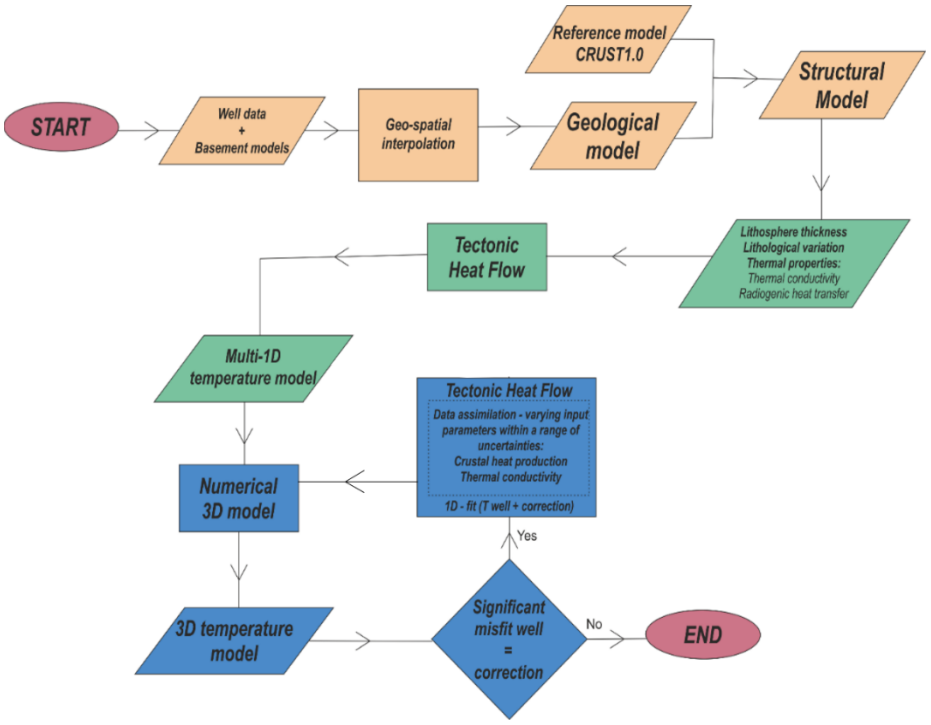

Figure 8. The workflow diagram of the modeling, including the structural, multi 1D thermal structure, and 3D thermal modeling

This study will aim to build the lithospheric-scale thermal model of the Central Sumatra Basin, focusing on the top few kilometers. The workflow of the study is shown in Figure 8. The first stage of the modeling is to build a geological model of the basin. This step is necessary to obtain the information regarding the structure and the lithological variation of the basin, which also determines the composition and the thermal properties for the modeling. After obtaining the information from the geological model, the temperature modeling will be performed using a Java program that has been developed, namely *Basin 3D Temperature* (B3T). Initially, a multi-1D temperature model in the 3D grid is calculated for the area, and the calculation will be based on 1D steady-state heat conductive method. This calculation will incorporate the petrophysical parameters such as pressure, temperature, porosity, and lithology based on the structural model. The output of the multi-1D temperature model will be used to compute the 3D temperature model. The thermal models will be iteratively calibrated, by modifying the uncertainties of the boundary conditions, so that the result will fit better to the observed

temperature. Data assimilation method will be performed to incorporate the observed temperature from the available wells, and they will be used to calibrate the 3D thermal model as well as to improve the thermal model.

3.1 3D geological modeling

In this study, the temperature modeling will be performed at a lithospheric scale, and it therefore requires a structural model of the area. This includes the outer structure of the Earth, such as sediments, upper crust, lower crust, and the lithospheric mantle (Figure 12). For the sedimentary layers, a geological model will be reconstructed using geospatial interpolation method, based on the available geological information from various sources in the area of the Central Sumatra Basin. For the layers below, including the crust and the lithospheric mantle, a reference model will be used to create the complete structural model. The result of the structural model, including the thermal properties, will be used as an input for B3T (*basin3dTemp.basin3dpreprocess sub-part of the program)* to calculate the prior multi-1D thermal model.

3.1.1 Sediments

No regional geological model of the Central Sumatra Basin are available. Therefore, as aprt of this study we will build a geological model of the area. Using geospatial interpolation, the model is based on the geological information from 185 wells (Figure 9) for the sedimentary units and the basement, and with addition inputs of the earlier basement models of the area for the basement (Nawawi, et al., 1996; Barber, et al., 2005).

For the geological modeling, the geospatial interpolation uses the information of the top depth of each sedimentary unit and the basement that were recorded on the wells, and this information is used to estimate the values of the depth in some other areas without wells. In general, the geospatial interpolation (Figure 10) function, F, is defined by Mitas & Mitasova, (2001) as:

$$F(r) = T(r) + \sum_1^m \lambda_j R(r, r_j) \quad (2)$$

where $r = (x, y)$ is a vector representing the location of the grid point, $r_j = (x_j, y_j)$ is the location of the wells, T is the pre-existing trend function (if any), λ_j is an interpolation coefficient, and $R(r, r_j)$ is a function of the distance between location point without well and location with well.

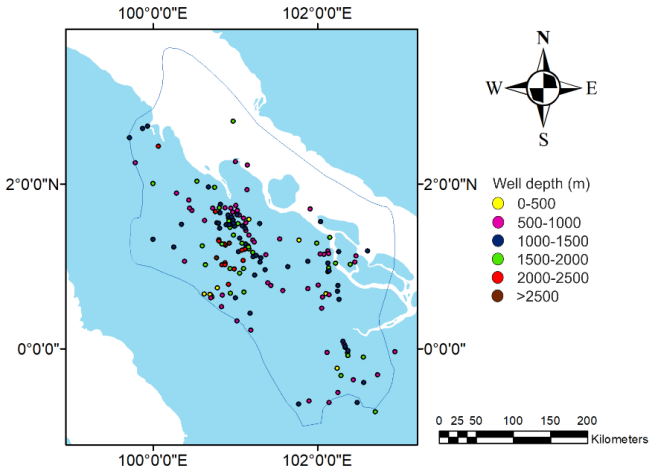

Figure 9. Map of wells distribution in the Central Sumatra Basin that contains geological information for the geological modeling

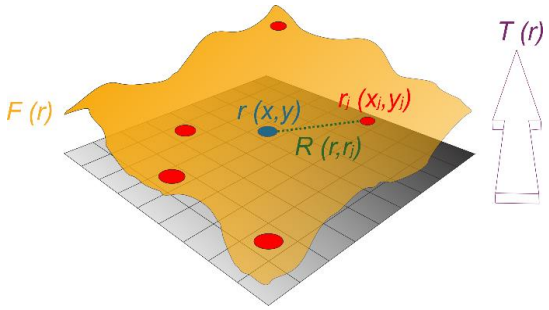

Figure 10. Schematic illustration of geospatial interpolation concept

For the sedimentary layer modeling, the spatial interpolation is based on a Triangulated Irregular Network (TIN) method. The method estimates the depth of the same layer in the area without wells, as a linear combination of values at three nearby points that form vertices of the triangle through Delaunay Triangulation (Mitas & Mitasova, 2001). Although the TIN method results in a continuous surface and it is more accurate than some other types of interpolation method (e.g., the Nearest Neighbors (NN)) (Li & Heap, 2014), the surface is created with abrupt changes in gradients as well as the high curvature at the margin of the triangles (Webster & Oliver, 2001). Therefore, a Kernel Smoothing method is adopted to minimize the overall abrupt gradient changes and surface curvature (Wand & Jones, 1995). This method resulted in a smoother surface that passes precisely through the data-points of wells locations (Figure 11).

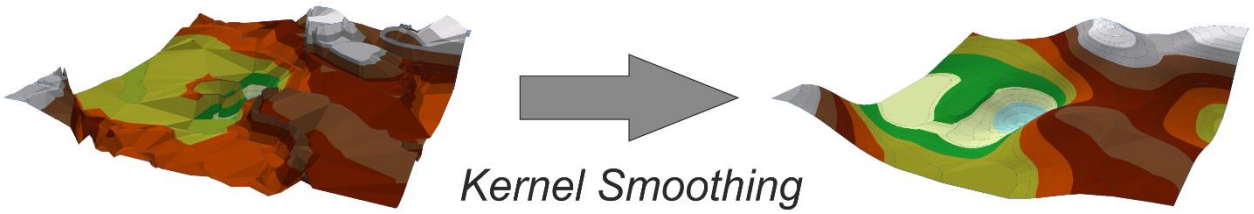

Figure 11. Schematic illustration of Kernel Smoothing

3.1.2 Crust and lithospheric mantle

The similar methods of geospatial interpolation are also applied to reconstruct the top surface of the basement, which also marks the upper part of the crust. Although the methods used are the same, the inputs for the basement modeling consist not only the geological information from the wells but also the digitized basement models from Nawawi et al. (1996) and Barber et al. (2005), which were compiled and reprocessed altogether to create a new basement model. For the information at the deeper part of the structure, including the lower crust, moho, and the lithospheric mantle, the reference model from CRUST1.0 by Laske et al. (2013) are adopted, in addition to other information obtained from Hall (2002).

3.2 Temperature modeling

The temperature model will be performed from the the surface down to the lithosphere-asthenosphere boundary (LAB) (Figure 12). This boundary is defined as the transition level from conductive (lithosphere) to convective (asthenosphere) heat transfer, where the corresponding temperature is 1315°C (McKenzie & Priestley, 2008). The numerical model will be performed on a regular 3D grid, with a horizontal grid spacing of 5 by 5 km (in an x-y direction), and varying vertical resolutions, with 100 meters for the uppermost 2.5 km (sedimentary layers) and 1 km down to the depth of the lithosphere (Figure 12).

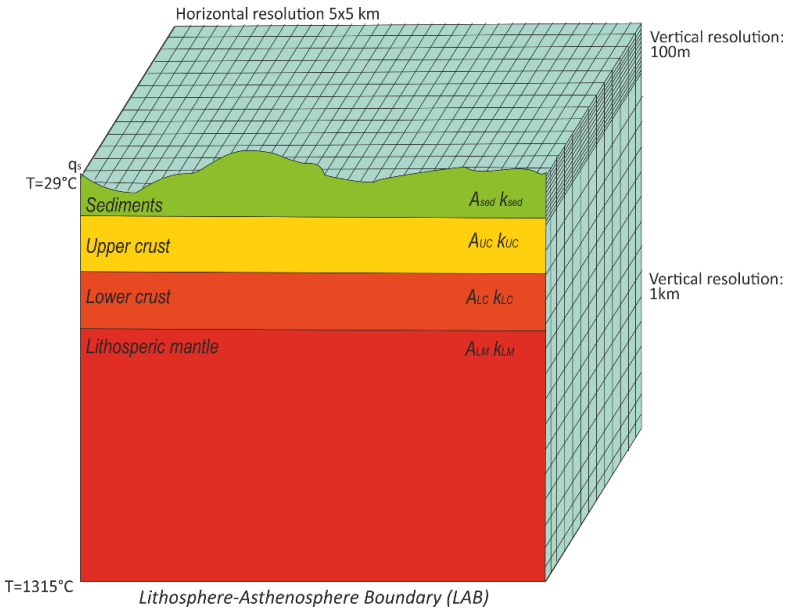

Figure 12. Simplified diagram of the structural layers of the lithosphere with several necessary inputs, such as heat generation (A), thermal conductivity (k), of the layers, and surface heat flow (q_s), and the horizontal and vertical grids

3.2.1 Temperature data

Temperature dataset from the measurements will be used to constrain the temperature calculation and results in the representative temperature model. In this section, the details of the temperature dataset will be discussed.

3.2.1.1 Temperature dataset types

The subsurface temperature measurements in the Central Sumatra Basin are obtained from oil and gas boreholes. Two types of temperature data from the available dataset are as follow:

- The Drill Stem Test (DST) is a procedure to test the well and formation by pumping fluids to the surrounding area of a borehole. This procedure provides information on the formation, such as pressure, temperature, permeability, and hydrodynamic information. In terms of temperature measurement, the injected fluid should be theoretically in thermal equilibrium with the surrounding formation, or at least very close to the temperature of the formation, with measurement error around $\pm 2°C$. However, the precision of the temperature measurement from this procedure can also be affected by particular circumstances, for example, due to sensor accuracy, flow or build-up during temperature measurement, or pressure drop during flow period (Bonté, et al., 2012). Therefore, these factors can increase the measurement error of the temperature measurement with this procedure, to $\pm 5°C$.
- The Bottom Hole Temperature (BHT) is usually a side-product of the logging tools. The data represents the maximum temperature measured during logging, which consider as the temperature at the bottom of the borehole. However, BHT is not in thermal equilibrium with the formation, because the logging operations are executed after the borehole was cleaned by the circulation of a colder mud, to remove the cuttings. The time elapsed between mud circulation and logging operation is relatively short, so the temperature in the borehole could not reach the thermal equilibrium with the formation. Such temperature perturbation, result in BHT being

colder than the actual formation temperature. Therefore, the correction for this type of dataset is necessary.

For this study, the temperature datasets that will be used consists of DST formation and corrected BHTs.

3.2.1.2 Correction methods of the BHT measurements

The temperature perturbation on the borehole measurements can be caused by either fluid circulation during the drilling or the cleaning of the borehole to remove the cuttings before the logging operation. Since the BHTs were measured at the bottom of the well, the significant thermal perturbations are most likely caused by the material circulation for cleaning the cuttings. Temperature corrections can be done in several different ways to provide a dataset of corrected BHT values (referenced as BHTx). In the order of a better precision of the correction, these methods are modeling correction, analytical correction, and statistical correction method.

The modeling correction method such as the one presented by Luijendijk et al. (2011) simulate the temperature of the borehole during drilling and the following return to the equilibrium. This method has the capability of solving the 2D heat flow equation. The result is also extremely precise, with a range of uncertainty around $\pm 5°C$. Although this method provides a compelling result of temperature correction, this method requires many parameters that the dataset provided for this study do not have. Therefore, this study will not use this method for temperature correction.

The analytical correction method is presented in Goutorbe et al. (2007). There are several types of analytical correction method that can be performed to solve the thermal perturbation and correct the BHT, with the uncertainty of $\pm 5 - 10°C$ (Goutorbe, et al., 2007). Each type of analytical correction method requires specific parameters to be able to calculate the correction. However, even with the correction types with the least amount of parameters, such as borehole radius, rock thermal diffusivity, and mud circulation time, this analytical correction seems to be impossible to perform for this study due to very limited information on the available dataset.

The statistical correction method (or known as AAPG statistical correction method), is based on an extensive database performed by Geothermal Survey of North America (GSNA) in the early 1970s. The database is built by 10,000 BHT data from about 20,000 boreholes in the USA, Canada, and Mexico, and they are compared to the DST available in the USA (Harrison, et al., 1983). The comparison was made to obtain a statistical correction using Eq. (1). Three sets of coefficients (Table 1) were defined by (Deming, 1989), where the first two datasets are defined for West Texas and Louisiana, and the third one is defined as an average, but can also be applied independently of the other two. The comparison between datasets corrected by AAPG statistical method and Instantaneous Cylinder Source (ICS) method, one of the types of analytical correction method, shows that the average bulk difference between the two is $3.7°C$, which is very acceptable. For this study, the AAPG statistical correction method will be performed to provide the corrected BHT dataset (referenced as BHTx_AAPG).

$$\Delta T = az + bz^2 + cz^3 + dz^4 \qquad (1)$$

Table 1. AAPG correction coefficients for West Texas and Louisiana (Deming, 1989)

Area	a	b	c	d
West Texas	-1.169×10^{-3}	-4.689×10^{-3}	6.609×10^{-10}	-8.312×10^{-14}
Louisiana	4.926×10^{-3}	2.164×10^{-3}	-7.628×10^{-10}	4.950×10^{-14}
Average	1.878×10^{-3}	8.476×10^{-7}	-5.091×10^{-11}	-1.681×10^{-14}

3.2.1.3 Temperature dataset of the Central Sumatra Basin

The area of Central Sumatra Basin is covered by numerous wells from hydrocarbon exploration and exploitation. The wells distribution does not cover the whole basin homogeneously. The areas with a high density of wells distribution are concentrated within the areas where the petroleum exploration and exploitation operate. These areas are the Central Deep, Kiri Through, Pematang Through, Bengkalis Through, Rokan Uplift, Balam Through, Sembilan Uplift, and Beruk High (Figure 6). Some other areas in the basin have very sparse wells distribution.

The temperature dataset for this modeling is originated from hundreds of the available well data which have been compiled by Hall (2002), and from IPA ATLAS of the Central Sumatra Basin, which was published in 1991. These available data are regrouped to create a single temperature dataset for this study. After omitting the unrealistic values and duplicates, the temperature dataset consists of 118 uncorrected BHTs from the measurements in 118 wells and 4 DSTs from the measurements in 4 wells, which are considered to have small measurement errors ($< 5^0C$). The BHTs are corrected for wells deviation and all the temperature maps in this paper show the projected XY position and the corrected depth.

3.2.1.4 Corrected temperature dataset for modeling

A correction method is applied to the uncorrected BHT measurements, to create a more reliable temperature dataset, or will be referred to as BHTx. The BHTs are corrected following the statistical correction method, or often referred to as AAPG correction method, described by Deming (1989). The result of the AAPG correction is a dataset of 118 BHTx_AAPG in 118 wells. The temperature values range from 250 m to 2500 m depth, where the drilling usually reached reservoir layer or top of the basement in the area of the Central Sumatra Basin. While the spatial distribution of the temperature dataset is related to the distribution of the wells in the Central Sumatra Basin (Figure 13), the vertical distribution of the temperature dataset is relatively homogeneous, with 46 values in the first 1 km, 67 values in between 1000 and 2000 m, and 9 values in between 2000 and 2500 m (Figure 14).

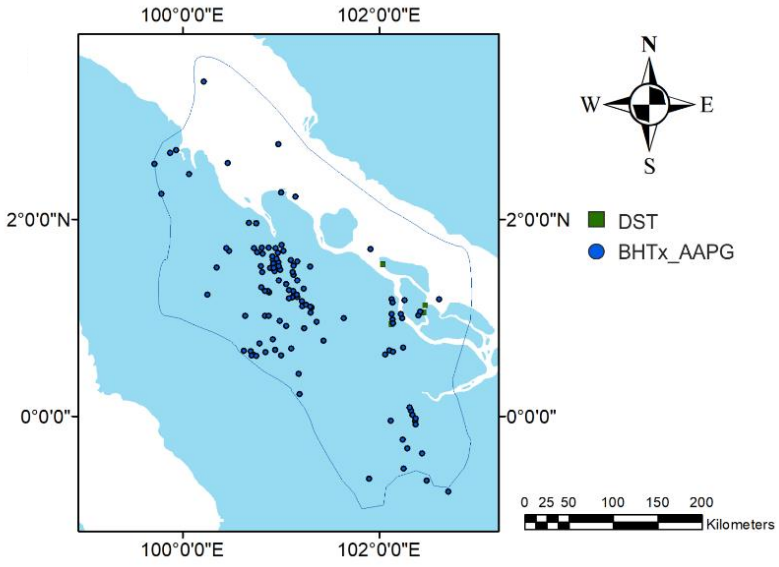

Figure 13. Map of the spatial distribution of the temperature data

The combined dataset of both DST and BHT values includes 122 values with a range of uncertainties. As mentioned earlier, the uncertainties for DST values are mostly related to the error caused by thermometer precision, which is about $\pm 5^0C$. On the other hand, the uncertainties for BHTx_AAPG are very challenging to determine without any reference to other correction methods. According to Deming (1989), the average bulk difference between BHTx_AAPG and BHTx_ICS (BHT values that are corrected by ICS method), is about

3.7^0C, while the uncertainties of BHTx_ICS is around 10^0C (Bonté, et al., 2010). With these references, the range of uncertainty can vary from 13.7^0C and even up to 15^0C (Harrison, et al., 1983). For this research, a range of uncertainty of 15^0C is adopted for BHTx_AAPG. According to the corrected temperature dataset, the average temperature gradient in the area is $52.2\ ^0C/km$, and the surface temperature is 29^0C (Figure 14).

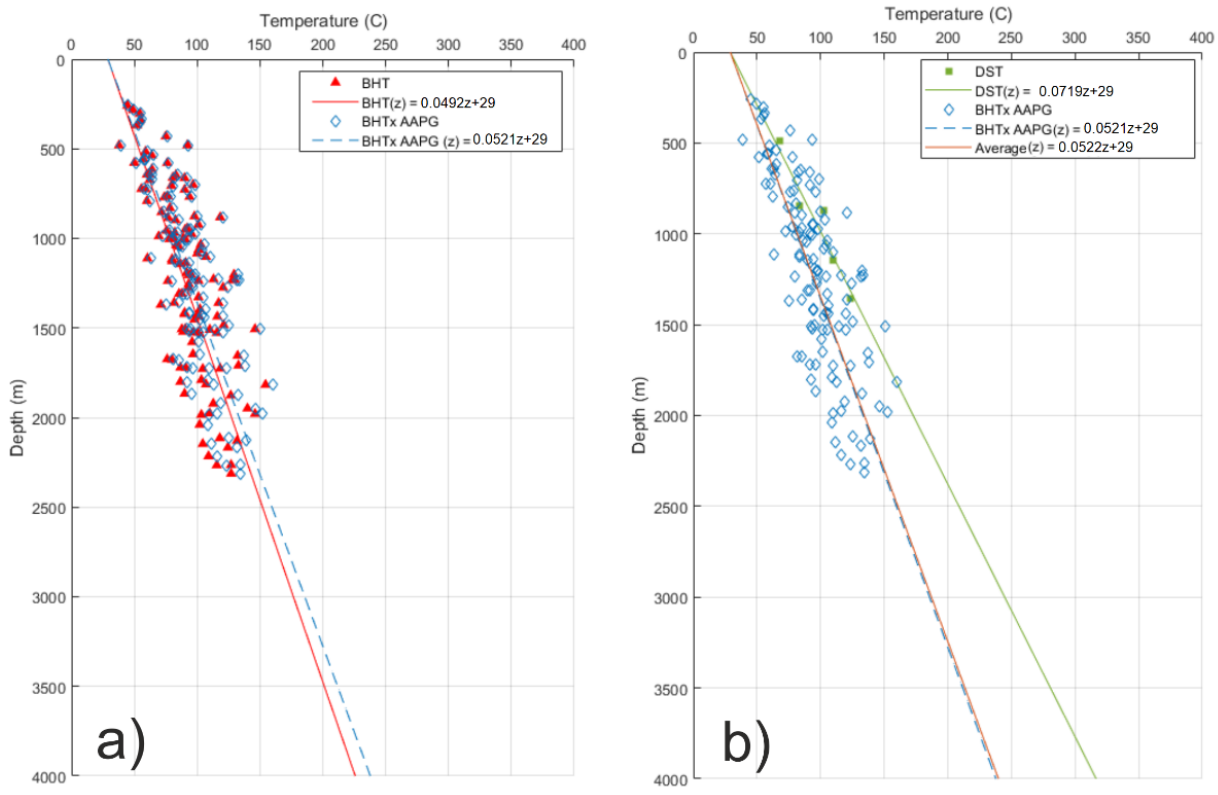

Figure 14. Comparison of temperature dataset between BHT and BHTx AAPG (a), BHTx_AAPG and DST (b) and a map wells locations where temperature data were measured

3.2.2 Modeling input

In this section, the details on the inputs used for the temperature modeling will be discussed, including the lithological definition for the sedimentary layers (3.2.2.1), and the thermal properties, such as thermal conductivity (3.2.2.2), and radiogenic heat production (3.2.2.3).

3.2.2.1 Lithological definition

Lithological variation needs to be defined to perform the temperature model, so the thermal properties such as thermal conductivities and the radiogenic heat production can be applied for the temperature calculation. The structural model will include four main layers: the sediment, the upper crust, the lower crust, and the lithospheric mantle.

The sediment layers are divided into several layers, following the regional stratigraphic unit of the Central Sumatra Basin, these layers, from the youngest to oldest, are Minas, Petani, Telisa, Sihapas, and Pematang. The simplified model of these sediment layers and their corresponding lithological variation is outlined in Table 2. The detailed description of each sedimentary unit is defined in 2.2. The deeper

structural layers are divided into the upper, lower crust, and lithospheric mantle, where the physical properties of each part are shown in Table 3.

Table 2. Overview of the sedimentary layers and their corresponding lithologies

No	Abbreviation	Layer Name	Period	Epoch	Age (Ma)	Lithology
1	MI	Minas Group	Quaternary	Pleistocene - Recent	0 - 2.8	20% Clastic Sediment Conglomerate Typical 40 % Clastic Sediment Sand Typical 40 % Clastic Sediment Shale Typical
2	PE	Petani Group	Tertiary	Middle Miocene - Pleistocene	2.8 - 13	25% Clastic Sediment Shale Typical 75% Clastic Sediment Sand Typical
3	TE	Telisa Group	Tertiary	Early to Middle Miocene	13 - 17.5	100% Clastic Sediment Shale Typical
4	SI	Sihapas Group	Tertiary	Early Miocene	17.5 - 25.5	25% Clastic Sediment Shale Typical 75% Clastic Sediment Sand Typical
5	PM	Pematang Group	Tertiary	Eocene - Oligocene	25.5 - 45	30% Clastic Sediment Shale Organic Typical 35% Clastic Sediment Sand Typical 35% Clastic Sediment Conglomerate Typical

Table 3. Overview of the crustal and lithospheric mantle parameters

Parameter	Unit	Value
Upper Crustal thickness	km	~ 16.8 - 22.8
Lower Crustal thickness	km	~ 3 - 15.4
Average Crustal thickness	km	~ 29.4
Upper Crustal density	kg m^{-3}	2700
Lower Crustal density	kg m^{-3}	2850
Lithospheric thickness	km	92.5
Lithospheric density	kg m^{-3}	3400

3.2.2.2 Thermal conductivity

In this section, the method used to calculate the thermal conductivity for each structural layer for this modeling. The overview of thermal conductivity values for each layer is shown in Table 4.

Table 4. Overview of thermal conductivity values used per layer

Layer	Thermal conductivity $[\mathrm{W.m^{-1}.K^{-1}}]$
Sediments	Different bulk values depend on lithological variation, compaction, temperature-dependence (Sekiguchi, 1984)
Upper crust	Pressure- and temperature-dependent (Eq. 8, (Chapman, 1986)
Lower crust	Pressure- and temperature-dependent (Chapman, 1986)
Lithospheric mantle	Lattice thermal conductivity (Xu, et al., 2004) and radiative thermal conductivity (Schatz & Simmons, 1972) (Eq. 9)

Sediments

Thermal conductivity, k, is defined as the ability of a particular material to transport heat, which varies depending on the lithological variation. The rock layers with a low thermal conductivity result in a steep temperature gradient, while the layers with higher thermal conductivity result in a gentler temperature gradient. However, the thermal conductivity for the same rock can be varying, due to several factors such as compositional and anisotropic variations, temperature dependence, and a change in the degree of compactions. The methodology from Hantschel & Kauerauf (2009) incorporate all these factors, and it will be adopted for the calculation of the thermal model. The anisotropy is incorporated, according to the Eq. 3:

$$\alpha_k = \frac{k_h^{20}}{k_V^{20}} \qquad (3)$$

where α_k is the anisotropy factor, $k_h^{20}$and k_v^{20} are the horizontal and vertical anisotropy at $20°C$, respectively. For specific lithologies, such as shale and limestone, the anisotropy factor can change during compaction, and subsequently affect the conductivity. This effect is defined as Eq. 4:

$$k_v(\phi) = k_{v0}\, f^{\frac{\phi}{\phi_c}} \qquad (4)$$

where f is a grain rotation factor, k_{v0} is vertical conductivity of a compact rock with ϕ=0 and ϕ_c is porosity after deposition (-). The value of f for shale and limestone is 1.38 and 1.11 respectively, while $f = 1$ is used for porosity-independent anisotropy. The porosity, ϕ, is based on Athy's Law:

$$\phi(z) = \phi_0 . e^{-Cz} \qquad (5)$$

where ϕ_0 is porosity at the surface, C is the compaction parameter, and z is depth. Temperature dependence of the rock matrix conductivity is defined by Sekiguchi (1984) in Eq. 5:

$$k_{h\ or\ v}(T) = 385\left(1.0227 k_{h\ or\ v}^{20} - 1.882\right)\left(\frac{1}{T} - 0.00068\right) + 1.84 \qquad (6)$$

where $k_{h\ or\ v}^{20}$ is either horizontal or vertical conductivity at $20°C$, and T is the temperature [K]. According to Hantschel & Kauerauf (2009), if the sedimentary unit consists of various mineral composition (for example, 50% of sand and 50% of shale), the conductivity value is calculated using the arithmetic mean for horizontal conductivity, and harmonic mean for vertical conductivity. The latter is used to obtain the bulk rock matrix conductivity, k_{brm} $[\mathrm{W.m^{-1}K^{-1}}]$, because it is more suited to represent the layered system of sedimentary infill in the basin, which is described as:

$$k_{brm} = \left(\frac{n}{\frac{1}{k_{brm1}} + [\dots] + \frac{1}{k_{brm2}}}\right) \qquad (7)$$

where n is the number of lithological components of the matrix thermal conductivity. Lastly, the bulk thermal conductivity of the sedimentary layer, k_{sed} $[\mathrm{W.m^{-1}K^{-1}}]$, is obtained by using the geometric mean of the thermal conductivity for the bulk rock matrix, k_{brm}, and for the pore fluid, k_w $[\mathrm{W.m^{-1}K^{-1}}]$, following the Eq. 8:

$$k_{sed} = {k_{brm}}^{1-\phi} . {k_w}^{\phi} \qquad (8)$$

where ϕ is the porosity calculated using the Athy's Law, with the value ranging from 0 to 1.

Crust

The values of thermal conductivity for the upper crust (k_{UC}) and lower crust (k_{LC}) are calculated following the incorporation of temperature- and pressure-dependence described by Chapman (1986), which is based on the real measurement of conductivity. The conductivity is defined as:

$$k_{UC\ or\ LC} = k_{UC\ or\ LC}^0 \left(\frac{1 + c.\sigma_{effz}}{1 + b.T}\right) \qquad (9)$$

where σ_{effz} is the effective lithostatic stress [MPa], and T is the temperature [K]. Table 5 shows the corresponding values of k^0, which is the thermal conductivity for either upper or lower crust at T=$0°C$ $[\mathrm{W.m^{-1}K^{-1}}]$, constants $c[\mathrm{km^{-1}}]$ and b $[\mathrm{K^{-1}}]$.

Table 5. Parameter values for crust thermal conductivity

Parameter	Upper crust	Lower crust
k^0	3	2.6
c	0.000053	0.000053
b	0.0015	0.001

Lithospheric mantle

As lithospheric mantle mainly consists of olivine, the thermal conductivity of lithospheric mantle, k_{LM}, is affected by two main processes, which are the electron-phonon-driven radiative heat transport, and the photon-driven lattice heat transport. With increasing temperature, the effect of the radiative component on thermal conductivity increases compared to the lattice component (Hofmeister, 1999). The equation for the temperature- and pressure-dependent lattice thermal conductivity, $k_{lat}\left(T, \sigma_{effz}\right)$, defined by Xu et al., (2004), and the temperature-dependent radiative thermal conductivity $k_{rad}\left(T\right)$, defined by (Schatz & Simmons, 1972), are used to calculate the thermal conductivity of lithospheric mantle, k_{LM} $[\mathrm{W.m^{-1}K^{-1}}]$, following the equation:

$$k_{LM}(z) = k_{lat}^{25}\left(T, \sigma_{effz}\right) + k_{rad}(T)$$

$$k_{LM}(z) = \sqrt{\frac{298}{T+273}}1 + 0.0032.\sigma_{effz} + 0.368.10^{-9}.(T+273)^3 \qquad (10)$$

where the k_{lat}^{25}, is the thermal conductivity $[\mathrm{W.m^{-1}K^{-1}}]$ of olivine at room temperature $(25°C)$ and at atmospheric pressure, T is the temperature $[\mathrm{K}]$, and σ_{effz} is the effective lithostatic stress, with the value of 4 GPa, representing the lithospheric mantle conditions as estimated by Xu et al., (2004).

3.2.2.3 Radiogenic heat production

Radiogenic heat production is caused by the decaying of radioactive isotopes in rocks such as uranium-238 (^{238}U), uranium-235 (^{235}U), thorium-232 (^{232}Th), and potassium-40 (^{40}K). Fixed values of radiogenic heat production, A $[\mu\mathrm{W.m^{-3}}]$, are used throughout the lithosphere. For sedimentary layers, a constant value of radiogenic heat generation will be based on the lithological variation. For the structure layers below the sediments, the constant values of $1\ \mu\mathrm{W.m^{-3}}$ for the upper crust (Hantschel & Kauerauf, 2009), $0.4\ \mu\mathrm{W.m^{-3}}$ for the lower crust (Hantschel & Kauerauf, 2009), and $0.02\ \mu\mathrm{W.m^{-3}}$ for the lithospheric mantle 0.02 (Hasterok & Chapman, 2011), are adopted for the temperature calculation (Table 6).

Table 6. Overview of radiogenic heat production values and thermal conductivities used per layer

Layer	Radiogenic heat production $[\mu\mathrm{W.m^{-3}}]$
Sediments	Different bulk values depend on lithological variation (Hantschel & Kauerauf, 2009) and compaction
Upper crust	1 (Hantschel & Kauerauf, 2009)
Lower crust	0.4 (Hantschel & Kauerauf, 2009)
Lithospheric mantle	0.02 (Hasterok & Chapman, 2011)

3.2.3 Temperature calculation and data assimilation

In this section, the method that was used to calculate the multi-1D temperature model (3.2.3.2), the 3D temperature model (3.2.3.3), and the procedure of data assimilation (3.2.3.4) will be discussed.

3.2.3.2 Multi-1D temperature calculation

The main objective of multi-1D temperature modeling is to populate each grid cell of the model, where the output will be reprocessed for reconstructing the 3D model. A steady-state conductive thermal

model is used to calculate the temperature solution for this modeling. Based on the information on the structural model and thermal properties, the multi-1D temperature solution is calculation within certain boundary conditions. These boundary conditions include the temperature at the surface of $29°C$, and lithospheric thickness, which marks the Lithosphere-Asthenosphere Boundary (LAB) and it corresponds to the temperature of $1315°C$. Before calculating the model, a depth range of lithosphere was subdivided in order of 100 m for the top 2.5 km, and 1 km for the deeper part. Initially, the temperature is calculated using a linear geotherm, following the average geothermal gradient of $52.2°C/km$. Later, the solution is calculated with the assumption that the heat flow Q is constant at the top of the interval, $z = z_0$, with constant thermal conductivity k and radiogenic heat production *A* (Eq. (11)):

$$T(z) = T_{Z_0} + \frac{Q}{k}(z - z_0) - \frac{A}{2k}(z - z_0)^2 \qquad (11)$$

Before the temperature calculation, heat flow is extrapolated to define the heat flow as a function of depth, $Q(z)$ $[\mathrm{W.m^{-2}}]$ from the top of the interval downwards (Limberger, et al., 2017a). The calculation is done by subtracting the integral of radiogenic heat production from the surface to a depth of z, $\int_0^Z A(\zeta)\, d\zeta$ $[\mathrm{W.m^{-2}}]$, with the equation:

$$Q(z) = Q_0 - \int_0^Z A(\zeta)\, d\zeta \qquad (12)$$

Based on the result of the calculated temperature solution, the thermal properties are updated, and the temperature solution is recalculated following the equations above (11 and 12). This process is iteratively done four times to subsequently result in a steady thermal properties solution and a priori temperature model, which will be used next for the forward 3D modeling.

3.2.3.3 3D temperature calculation

For the 3D forward modeling, the temperature calculation will use the prior temperature model and the thermal properties (thermal conductivity and heat production). The boundary conditions, which include surface temperature and the depth of LAB from the multi-1D temperature (as the outcome of *basin3dTemp.basin3dpreprocess*), will be used to calculate the 3D temperature model using a finite-difference approximation. The model solves the heat equation for steady-state conditions with the equation:

$$\rho c_t . \frac{\partial T}{\partial t} = \nabla . (k_t . \nabla T) + A \qquad (13)$$

where the ρ is the density $[\mathrm{kg.m^{-3}}]$, c_t is the specific heat capacity $[\mathrm{J.kg^{-1}.K^{-1}}]$, T is temperature $[\mathrm{K\ or\ °C}]$, k_t is thermal conductivity $[\mathrm{W.m^{-1}K^{-1}}]$, A is radiogenic heat production $[\mathrm{W.m^{-3}}]$, and ∇ is the nabla operator: $\left(\frac{\partial}{\partial x}, \frac{\partial}{\partial y}, \frac{\partial}{\partial z}\right)$ (e.g., van Wees et al., 2009). The model volume extends across the area and vertically ranges up to 187 km depth. The volume is discretized in horizontal extent at a 5 km resolution. For the vertical resolution, a resolution of 100 m is used for the top 2.5 km, where the sedimentary units, while a resolution of 1 km is used in the greater depth. The discretion problem creates a significant set of linear equations, which is solved by the Preconditioned Conjugate Gradient (PCG) method (Guo & Langevin, 2002).

3.2.3.4 Data assimilation procedure

The result of the temperature model requires calibrations in order to make it a representative model of the actual temperature. Data assimilation method is performed to update the existing prior thermal

model and thermal properties and to make them as representative as possible subsequently. The corrected temperature dataset is adopted as the main target of the observation. The workflow of the data assimilation procedure is schematically outlined in Figure 15. First of all, calculating thermal requires several input parameters that have a specific range of uncertainties. These input parameters consist of thermal conductivity, k, for the sedimentary units (at the top few kilometers), radiogenic heat production, *A*, in the upper crust, and the temperature at the lower boundary condition (LAB). By using the pre-updated (prior) parameters, the prior thermal model is calculated within a specific range of uncertainty. On the other hand, the corrected temperature dataset from measurement also has a specific range of uncertainties. A model misfit indicates the difference between the modeled and the observed temperature, in which the uncertainties for both temperature data, has an overlapping area (Figure 11). In order to minimize the misfit between the two, the prior thermal model will be updated, with observed temperature as a target observation. Using Ensemble Smoother Multiple Data Assimilation (ES-MDA) method according to (Emerick & Reynolds, 2013), the input parameters are varied within their uncertainties, to calculate the updated (posterior) thermal models that fit better to the observed temperature, with a smaller misfit between the two. The model can be improved by varying all input parameters all at once, but it can also be done in sequence. For this research, the input parameters are varied sequentially (Table 7).

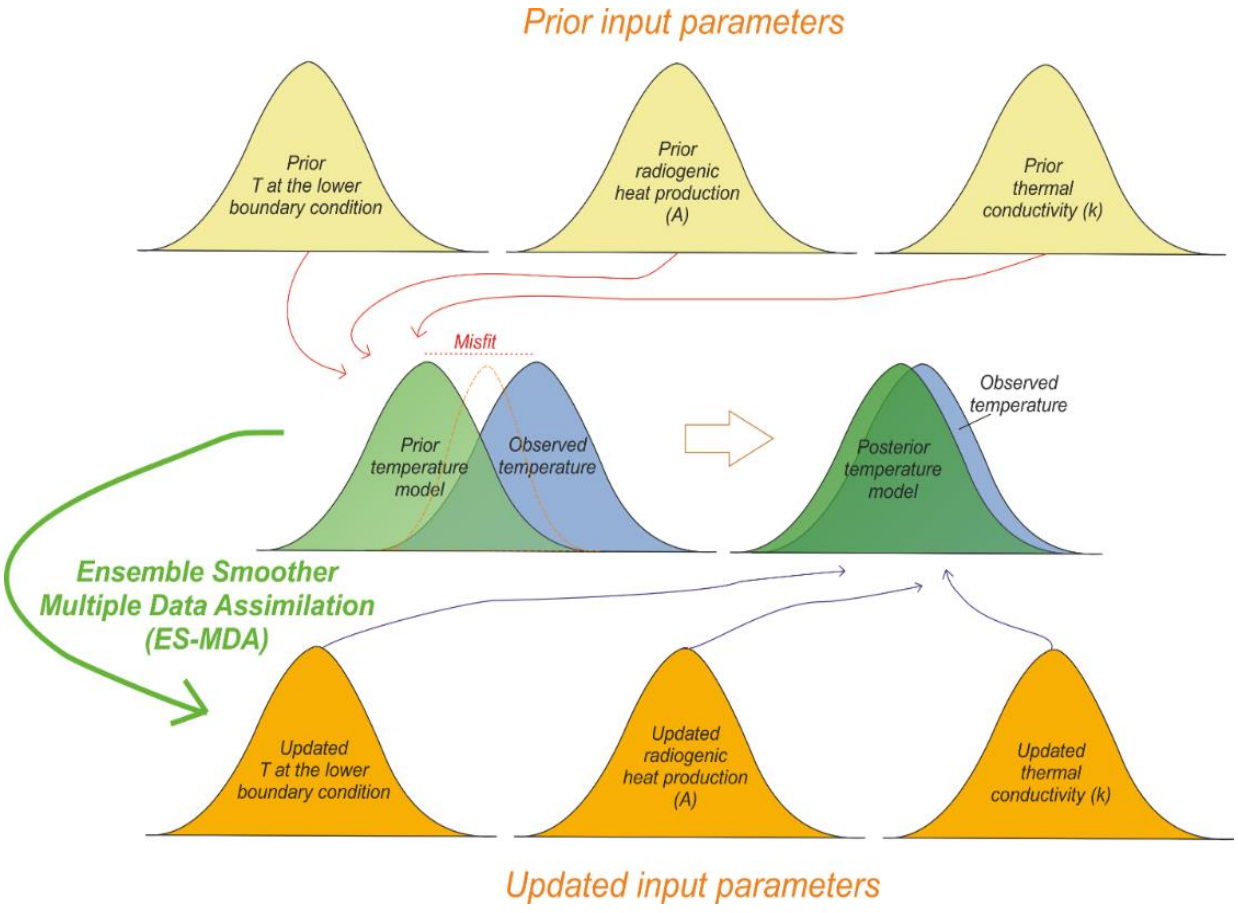

Figure 15. The workflow diagram of the data assimilation procedure (After Limberger et al., 2017a)

Table 7. Description of multiple sequences used for ES-MDA method: this sequence includes the variation of thermal conductivity (KV) and radiogenic heat production (A)

Scenarios	Description	Variogram in cells (1 cell ~ 5 km)	Runs in ensemble	Number of iteration	Pre-defined bandwidth for scaling parameters (by scaling and shifting)
1	Prior thermal model (No DA)	-	-	-	-
2	Varying KV only (for all sediments layers)	KV = 5	100	4	KV: scale in between 0.2-2
3	Varying A only (for upper crust)	A = 10	100	4	A: scale in between 0.2-3
4	Varying KV (for all sediment layers) and A (for the upper crust)	KV = 5 A = 10	100	4	KV: scale in between 0.2-2 A : scale in between 0.2-3
5	Varying KV (for all sediment layers) and A (for the upper crust)	KV = 10 A = 15	100	4	KV: scale in between 0.2-2 A : scale in between 0.2-3

4 Result

4.1 Structural model

The subdivision of sediment layers in the Central Sumatra Basin is shown in the geological model in Figure 16 in the form of the top structure map of each stratigraphic unit. According to various sources, the Tertiary basement of the Central Sumatra Basin is dominated by greywacke, quartzite, and granite, and the deepest top basement is around 2.4 km. The oldest sedimentary unit in the area is Pematang Group, which was deposited as a syn-sedimentary unit. The unit is dominated by clastic sediment conglomerate type and organic silt, with varying thickness from 3 to 579 m. The thickest part of the unit is associated with the sub-basins or the lowland areas of the basement, such as Central Deep, Kiri Trough, Bengkalis Trough, Mandian Trough, Barumen Basin, and Rokan Trough. This unit is confined by the highland areas of the basement such as Sembilan Uplift, Minas high, Beruk High, Dumai High, Kampar High, and the margin of the basin. The overlying Sihapas group, which consists of mainly sand and shale, has an average thickness of 278 m. Some parts of this unit conformably overlie the Pematang Group, while some other parts are unconformably deposited above the basement. The Sihapas group is overlain by Telisa Group, which is mostly dominated by shale, with an average thickness of 295 m. The following unit, the Petani Group, is dominated by sand at the bottom and shale at the top, with an average thickness of 220 m. The youngest stratigraphic unit in the area, Minas Group, has an average thickness of 94 m and consists of mainly shale, sand, and gravel at the upper part of the unit.

For the lower layers, including the upper crust, lower crust, and the lithospheric mantle, a reference model from CRUST1.0 from Laske et al. (2013) was adopted, in addition to information obtained from Hall (2002). The model also includes the structure layers that separate each layer, such as the top of the lower crust, moho, and Lithosphere-Asthenosphere Boundary (LAB). According to the model from Hall (2002), the thickness of the crust in the area of Central Sumatra Basin in 92.5 km.

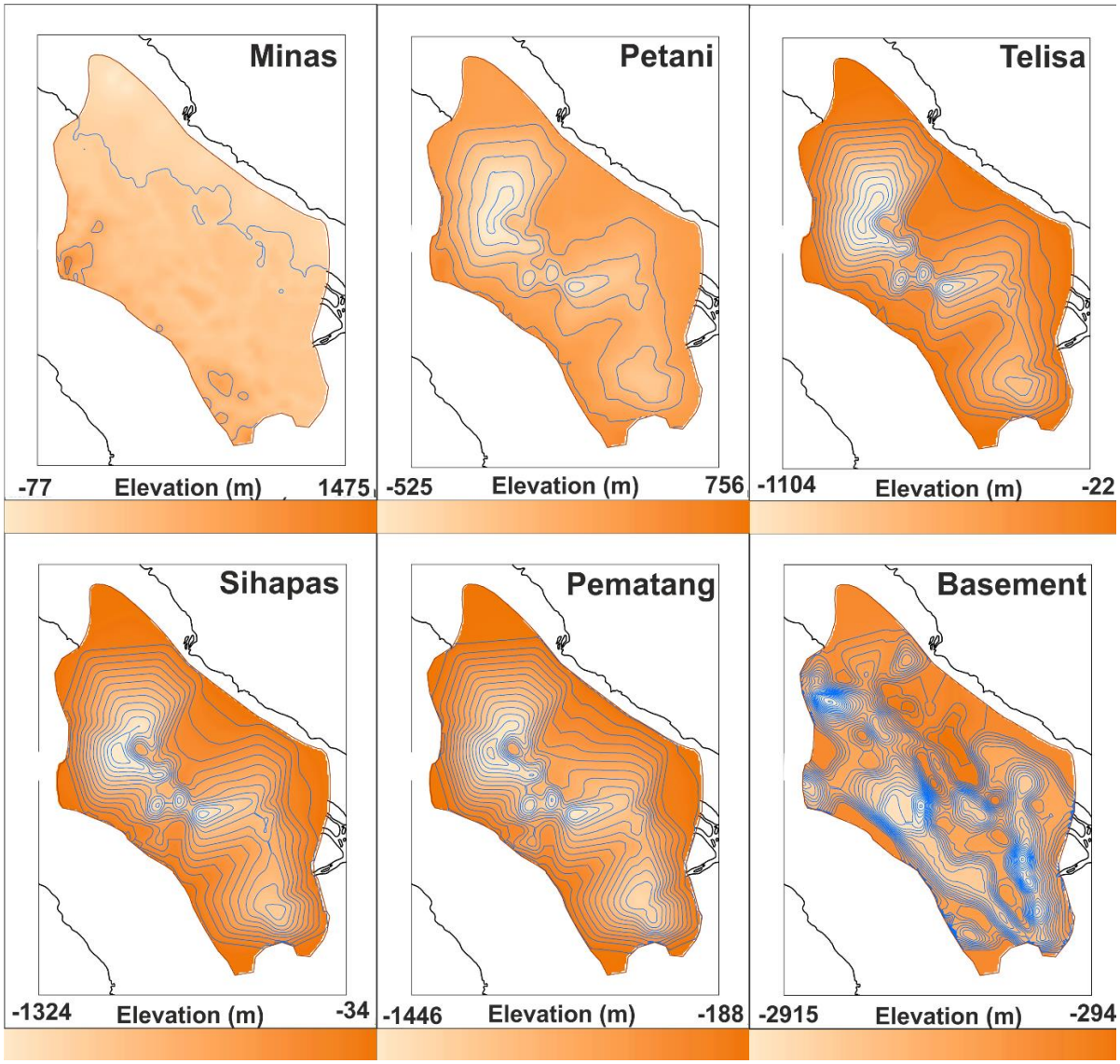

Figure 16. 3D geological model of the Central Sumatra Basin, showing the top structure map of each stratigraphic unit: Minas, Petani, Telisa, Sihapas, and Pematang, as well as the top of the basement

4.2 Temperature model

4.2.2 Initial prior thermal model

The 3D temperature model was calculated by using the input from the multi-1D temperature model without constraining the observed temperatures. The initial 3D thermal model is calculated using the modeling inputs (see 3.2.2), as well as the 3D geological model for the upper structure, and the adopted global reference for the lower structures (see 4.1). The result of the initially calculated 3D temperature model is shown in Figure 17 as the iso-depth maps of the temperature at a depth of 500 m, 1000 m, 1500 m, 2000 m, and 2500 m. The result that was calculated without constraining the observed temperature, including this initial model, will be referred to as a 'prior thermal model.'

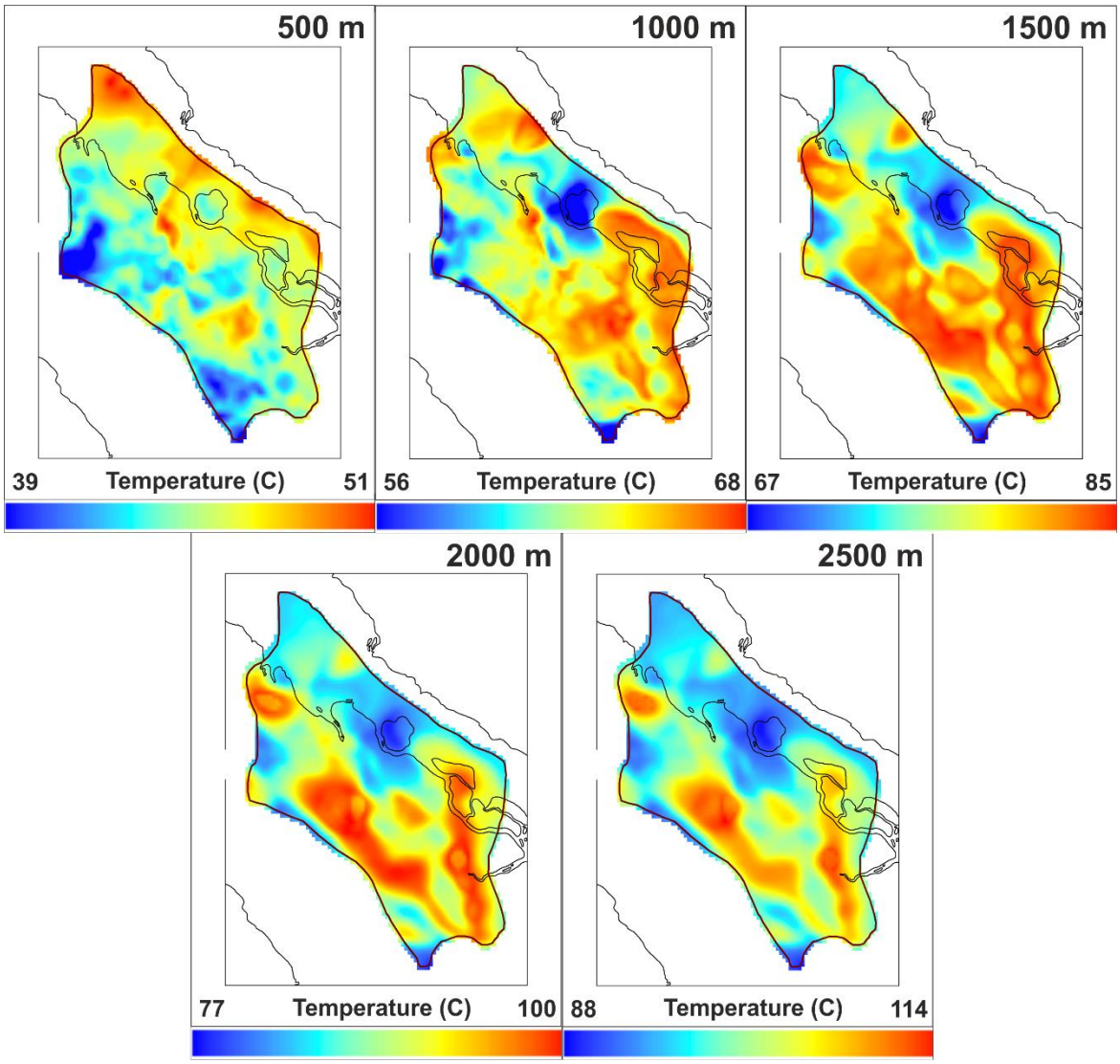

Figure 17. Result of the 3D forward temperature model (prior model), showing the iso-depth maps of temperature at depth 500 m (a), 1000 m (b), 1500 m (c), 2000 m (d), and 2500 m (e)

The result of the initial prior thermal model is evaluated to determine whether or not the model is sufficiently representing the actual temperature condition in the area. The thermal model evaluation uses the temperature observation from 122 wells, where the majority of the observation are obtained from the corrected BHT (BHTx_AAPG), and 4 values are obtained from the DST. Theoretically (but not necessarily), a representative model should have a very small misfit between the model and the observation, or quantitatively as close to 0 as possible. However, in this case, the initial prior thermal model has an average misfit of -24.467 °C (Figure 18), which means that the model underestimates the observed temperature in the area, or in other words, the model is too cold to represent the temperature of the area.

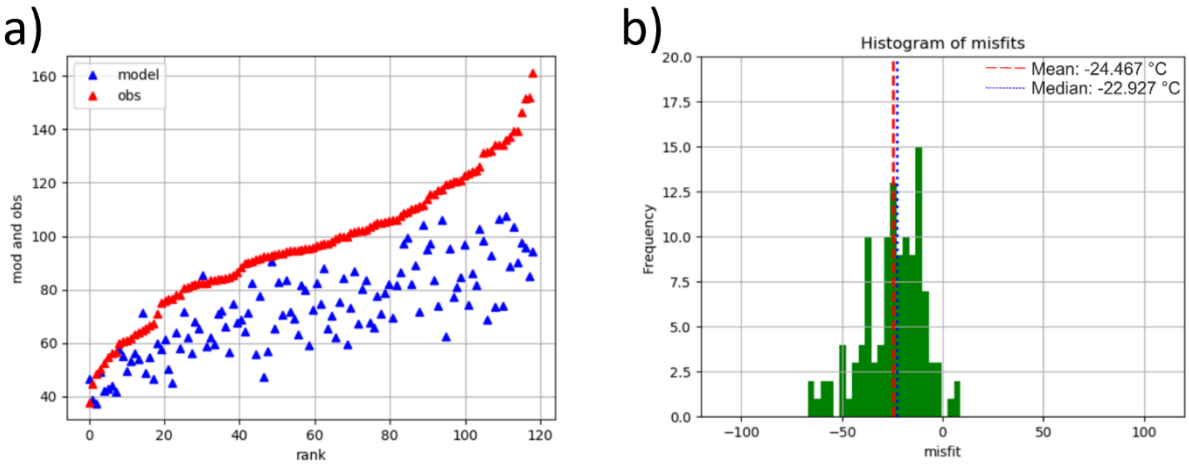

Figure 18. Comparison graph of the observed and modeled temperature (prior model) (a). Histogram of misfits between the prior thermal model and temperature observations (b)

4.2.3 Sensitivity analysis

Due to a significant average misfit between the initial prior thermal model and the observed temperature, a sensitivity analysis was performed to examine the effect of lithospheric setting on the temperature model. Two most plausible factors that have a considerable impact on the 3D thermal model are the upper crust composition and the lithosphere thickness. In this section, the effects of each factor on the sensitivity of the thermal model will be discussed.

4.2.3.2 Effect of the upper crust composition

The upper crust mainly consists of granite, which can produce heat production due to the radiogenic elements. Different types of granite have different thermal properties, or more specifically, the radiogenic heat production. The younger granites have higher radiogenic heat production and can generate more heat than the older granites. For this modeling, four types of intrusive granites as the main composition of the upper crust were defined by Hantschel & Kauerauf (2009). The sensitivity analysis will include all four types of upper-crust granite with different radiogenic heat production, and it is shown in Table 8.

Table 8. Four different types of granite used for sensitivity analysis

ID	Details	Radiogenic heat production (A) [μW/m³]
OldGranite	Typical old granite for cratons	1
Granite1000	Granite >1000 Ma	2.25
Granite500	Granite >500 Ma	2.57
Granite150	Granite >150 Ma	3.32

The effect of different upper crust granite is shown in Figure 19, and the result clearly shows that the misfit between the modeled and observed temperature decreased with the younger granite, which has higher radiogenic heat production. The heat production for the typical upper-crust granite for craton is too cold for the model. On the other hand, the better fits are obtained by using Granite 1000, Granite500, or Granite150 (Figure 19).

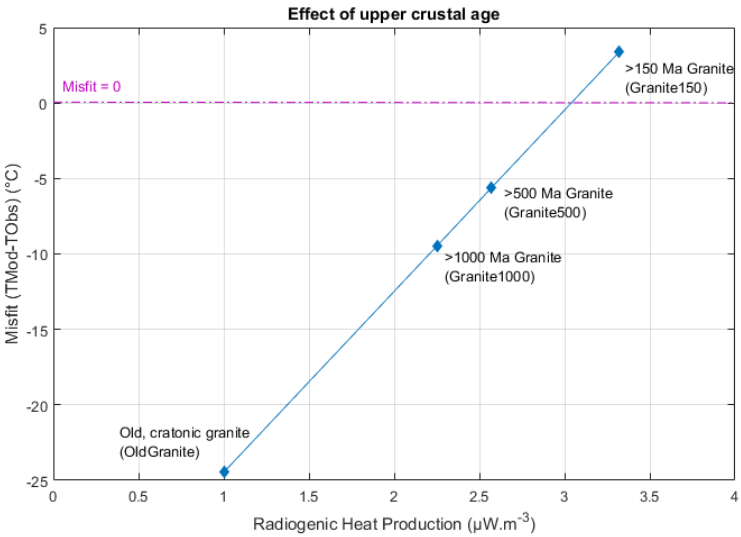

Figure 19. The comparison of the average misfit for different types of upper-crust granite (A typical cratonic-, >1000 Ma-, >500 Ma-, and >150 Ma-granite)

4.2.3.3 Effect of the lithosphere thickness

The lithosphere thickness plays an essential role in producing significantly high temperature and heat flow. Thinner lithosphere thickness is associated with the higher temperature or heat flow, while the thicker lithosphere thickness is associated with the opposite. In this section, the sensitivity analysis will include several numbers of lithosphere thickness: 92.5 (Hall, 2002) 70.6 (Laske, et al., 2013), 60, 55, 50, 45, 40, and 35 km as the average depth of Moho in the area according to Laske et al. (2013).

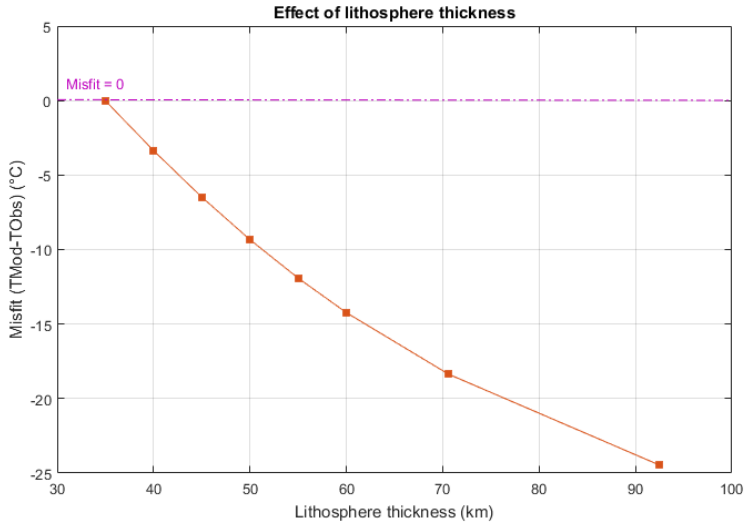

Figure 20. The comparison of the average misfit for various numbers of lithosphere thickness

The effect of lithosphere thickness is shown in Figure 20, and the result shows that the misfit between the modeled and observed temperature decreased with the thinner lithosphere thickness. The biggest misfit is shown by using the lithosphere thickness of 92.5 km, which was used for the prior thermal

model, while the smallest misfit is obtained by using the lithosphere thickness of 35 km, which represent the most extreme case of lithospheric stretching.

4.2.3.4 Preferred lithospheric configuration

The temperature model is highly sensitive to both upper-crust composition and lithospheric thickness, as shown by the sensitivity analysis above. In this section, three lithospheric configurations were set up: the thinnest- (i), the moderate- (ii), and the thickest-lithosphere (iii) (Table 9). For each configuration, the variation of the upper-crust granites will be applied to determine which combination that can result in the best-fit thermal model with the lowest misfit.

Table 9. Three different model scenarios of lithospheric configuration

Lithospheric configuration	LAB (km)	Moho (km)	Top lower crust (km)
1 (thinnest)	30	15	10
2 (moderate)	50	20	15
3 (thickest)	90	30	25

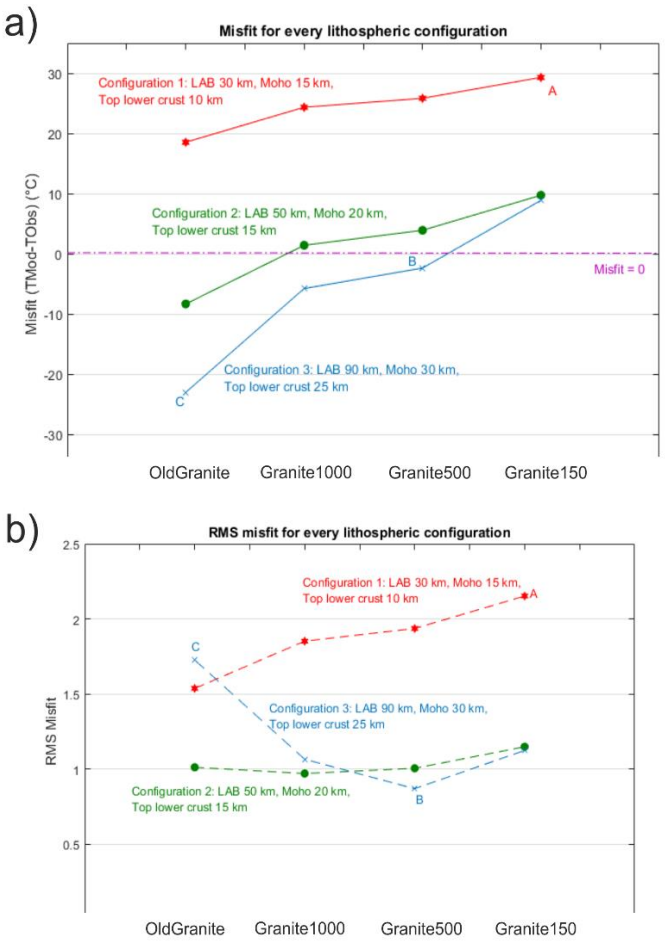

Figure 21. The comparison result of misfit values (a) and the RMS misfit (b) between modeled and observed temperature for each scenario (i, ii, and iii) with different upper-crust granites (OldGranite, Granite1000, Granite500, Granite150)

Figure 21 shows the comparison result of misfit values between modeled and observed temperature for each scenario with different upper-crust granites. The result shows that for every different type of upper-crust granite, the thinnest lithospheric configuration results in the overestimated models. The smallest misfit value for this configuration is 18.525 °C, which was obtained by using the oldest granite ('OldGranite'), while the highest misfit was obtained by using the youngest granite ('Granite150'), with the misfit value of 29.300°C. For the moderate lithosphere case, the misfit values are varying from the underestimation of -8.349°C for the 'OldGranite' to the overestimation of 9.721°C for the 'Granite150.' For the thickest lithosphere case, the misfit values are also varying from -23.042°C for the 'OldGranite,' to 8.868°C for the 'Granite150.' The best misfit for this scenario, which is -2.377°C, is achieved by using the 'Granite500.'

From this lithospheric configuration, three prior temperature models are

selected as frameworks for inverse 3D modeling. The detail of each selected model is shown in Table 10. Model A refers to the model with the most overestimation and highest value of misfit average (RMS = 2.15). Model B refers to the model that closely-estimates the actual temperature in real life with the best misfit average (RMS = 0.97). Model C refers to the model with the most underestimation and the lowest value of misfit average (RMS = 1.72). In the next section, the data assimilation method will be performed to these selected models by incorporating the variation of thermal properties.

Table 10. Details on three selected models as frameworks for the inverse 3D modeling

Model	Lithospheric configuration	LAB (km)	Moho (km)	Top lower crust (km)	Upper crust setting (granite type and the radiogenic heat production, A)
Model A – Highest model	1 (thinnest)	30	15	10	Granite >150 Ma (A=3.32 µW/m^3)
Model B – Closest model	3 (thickest)	90	30	25	Granite >500 Ma (A=2.57 µW/m^3)
Model C – Lowest model	3 (thickest)	90	30	25	Typical old, cratonic granite (A=1 µW/m^3)

4.2.4 Model scenarios

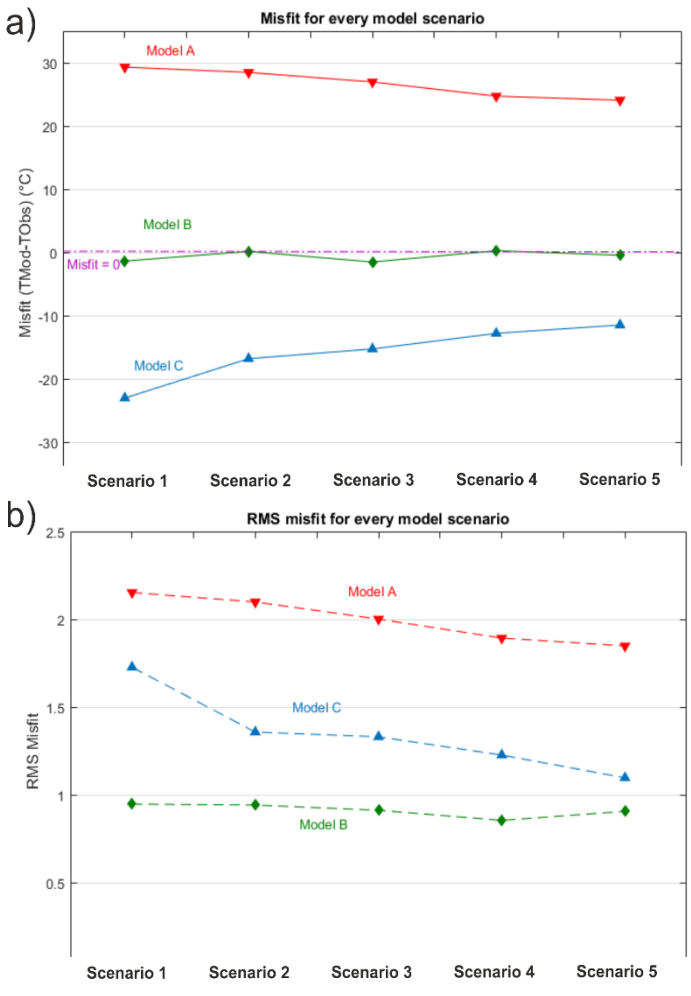

Figure 22. The comparison result of misfit values (a) and the RMS misfit (b) between modeled and observed temperature for each scenario (1, 2, 3, 4, and 5) with different selected models (A – Highest model, B – Closest model, and C – Lowest model)

The analysis of model scenarios was performed to evaluate the different thermal models and to determine the best-fit thermal model that can represent the actual temperature condition. Two groups of model scenarios were designed to examine the effect of lithospheric setting and the thermal properties on the thermal model. The first group of model scenarios will examine the effect of different lithospheric settings by using forward 3D modeling, while the second group of the model scenarios will examine the effect of thermal properties variation by using inverse 3D modeling.

The thermal properties, such as thermal conductivity (KV) and radiogenic heat production (A), can have a significant effect on the temperature model. In this section, inverse 3D modeling will be performed through data assimilation process for the three selected models from the previous section (Table 10). For model A and C, this method is applied to examine whether or not the thermal properties variation has a significant impact on compensating the big misfits resulted from the lithospheric setting. For model B, this method is applied

to update the pre-existing model and to obtain a new model with a better misfit compared to the current model. For every selected model, several scenarios were performed based on the variation of thermal properties, and the details for each model scenarios are described in Table 7.

Figure 22 shows the comparison result of misfit values between modeled and observed temperature for every selected model in different scenarios. In model A and C, the variation of thermal properties affected the misfit of the model. The most significant misfit change for both models is achieved in scenario-5. This scenario scales the KV for all sedimentary layers within the range of 0.2 to 2 with the smoothing radius of 50 km and scales the A for the upper crust within the range of 0.2 to 3 with the smoothing radius of 75 km. The average misfit values for model A5 (model A, scenario 5) and model C5 (model C, scenario 5) are 24.069 ^{o}C and -11.492 ^{o}C, respectively. However, even with the scenario that resulted in the smallest misfit for both model A and C, the misfit value is still far too significant, which indicates that the lithospheric setting has a more dominant impact on the thermal model, as opposed to the variation of the thermal properties. On the other hand, the 'best' misfit average for model C was also achieved by performing scenario-4 (model C4). The average misfit value for model C4 is 0.2663^{o}C, and the RMS misfit is 0.85, which indicate that the model is reasonably representative.

4.2.5 Preferred model

The best thermal model is shown in model C4 (Model C, Scenario 4), which corresponds to the lithosphere setting as follow: the lithospheric thickness of 90 km, Moho depth of 30 km, the top lower crust at 25 km, and the upper crust consists of >500 Ma granite with radiogenic heat production of 2.57 μW/m^3. This model also corresponds to the variation of calibration parameters, including KV and A (Details on scenario-4 in Table 7). The model has the smallest misfit compared to all the other models, which is 0.2663^{o}C (Figure 23), and it is selected as the preferred model to represent the actual temperature condition in the area. The model is presented in Figure 24 as the maps of the temperature at a depth of 500 m, 1000 m, 1500 m, 2000 m, and 2500 m. These maps are superimposed by well data distribution, where the temperature measurements were observed.

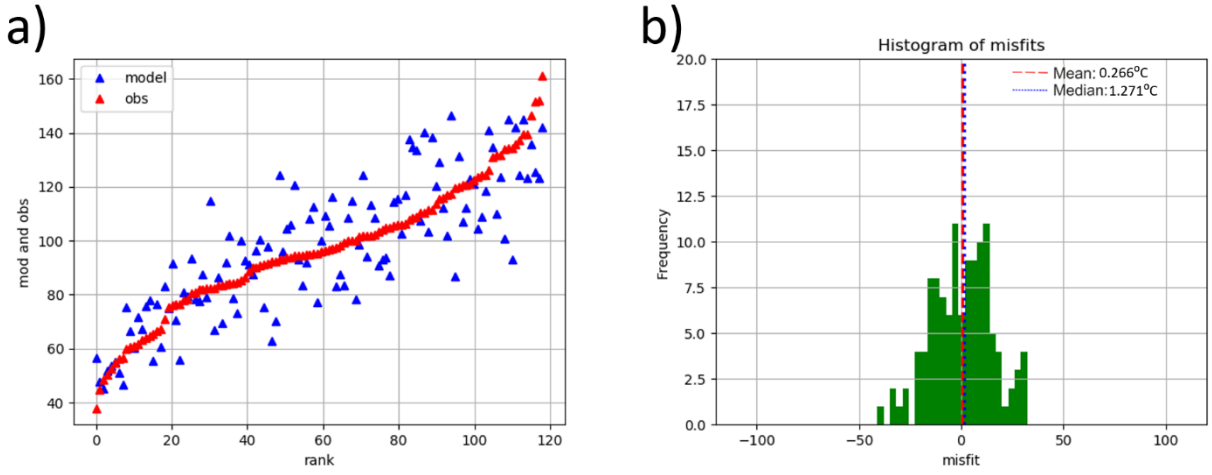

Figure 23. Comparison graph of the observed and modeled temperature (preferred model) (a). Histogram of misfits between the preferred thermal model and temperature observations (b)

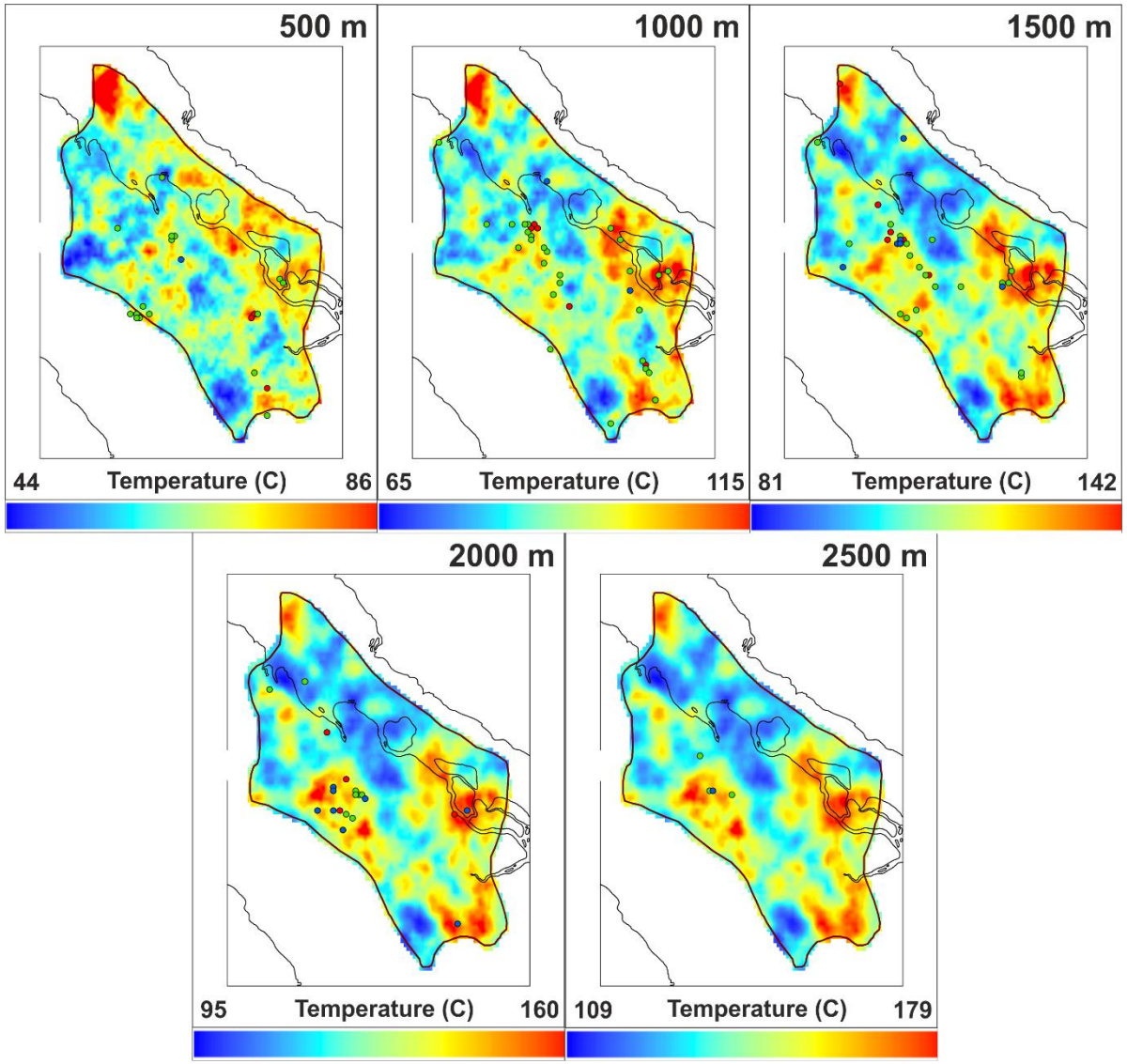

Figure 24. Result of the preferred temperature model, showing the iso-depth maps of temperature at depth 500 m (a), 1000 m (b), 1500 m (c), 2000 m (d), and 2500 m (e). These maps are superimposed by well distribution in which the observed temperature data were obtained. The temperature data on the wells are divided into three categories: the observed temperature that is closely-estimated (green), overestimated (blue), and underestimated (red)

5 Discussion

5.1 Effect of lithospheric setting on the temperature anomaly

The temperature model is significantly affected by changing the parameters of the lithospheric configurations, including the lithospheric thickness and the upper crustal heat generation. The local variation of these parameters is likely to affect the misfit between the modeled and the observed temperature.

The initial prior thermal model uses the lithosphere thickness of 92.5 km and the typical old, cratonic granite for the upper crust as the lithosphere setting. Even though this setting is most commonly used for the area, it leads to a significant misfit of modeled and observed temperature, which also indicates that this setting is not suitable for the area. The best result is achieved by using the lithospheric thickness of 90 km, which is slightly thinner than the original thickness, and the >500 Ma granite, in which the heat production is substantially higher than the typical cratonic granite. This setting compensates for the significant temperature difference between the model and the observation, indicating that the lithospheric configuration is suited for the area.

The best thermal model result is achieved by using the lithosphere thickness of 90 km as a part of the lithospheric setting. The suggested lithosphere thickness of the model is also in agreement with the tomographic data by Hall & Spakman (2015), also with the Yu et al (2017), stating that the lithosphere thickness of the area of the Central Sumatra Basin is approximately 90 km. The lithosphere thickness suggested by the model is thinner than the average of the typical continental lithosphere thickness, which is approximately 100-125 km (Rychert & Shearer, 2009), and it is also thinner than the number suggested by Hall (2002), which is 92.5 km. Consequently, the relatively thin lithosphere thickness partly contributes to a high-temperature anomaly in the area and it most likely occurs as a response to isostasy, which was triggered by the opening of the Sumatran back-arc basins, including the Central Sumatra Basin. Such geodynamic development is often associated with the Great Sumatran Fault and the Indo-Australian plate subduction towards the Sundaland (Pubellier & Morley, 2014; Zahirovic, et al., 2014).

The age of the upper crust in Sumatra is still not very well constrained, as it is poorly exposed and there is a lack of geological information at the depth greater than 2.5 km. Various studies on Sumatran granites suggested the age of the granites are ranging from 203 Ma to 5 Ma (Eubank & Makki, 1981; Barber, et al., 2005). However, these granites are associated with the volcanic arcs from different tectonic cycles throughout the geological time. Other sources suggested that the age of the crystalline basement of the Sumatra can be as old as Proterozoic, approximately ~1 Ga (Jones, 1961; Hutchison, 1994; Barber, et al., 2005). This notion is supported by the discovery of the Proterozoic rocks in the Malaysian Langkawi Islands, which is relatively close to the area of the Central Sumatra Basin (Jones, 1961; Barber, et al., 2005). Therefore, the age of the Sumatran upper crust can be within the extended time range of 203 to 1000 Ma.

From the Paleozoic (541 Ma, pre-Devonian) to Early Triassic (201 Ma), Sumatra underwent several major tectonic events (see 2.1) such as block separation from the East Gondwana, crustal accretion of the Sibumasu and Cathaysia block, and Sumatran orogenesis (Barber, et al., 2005). These events might have led to crustal reworking and partial melting that caused the differentiation of the Sumatran upper crust to increase progressively, since the heat-producing elements preferentially partition into the melts, due to their incompatibility (Workman & Hart, 2005; Gard, et al., 2019). Consequently, the increase in heat production can be expected from the old Sumatran upper crust (pre-Events, ~>1000 Ma) to the younger

upper crust (during- or post-Events, 541-201 Ma). This tectonic setting is sufficiently represented in the model C4, with the upper crustal consists of >500 Ma granite. The typical granite in this age has the radiogenic heat production of 2.57 µW/m^3, which is more than twice higher than the typical old cratonic granite with the radiogenic heat production of 1 µW/m^3. Consequently, the higher upper crust heat production post-crustal reworking contributes to a higher temperature anomaly in the area.

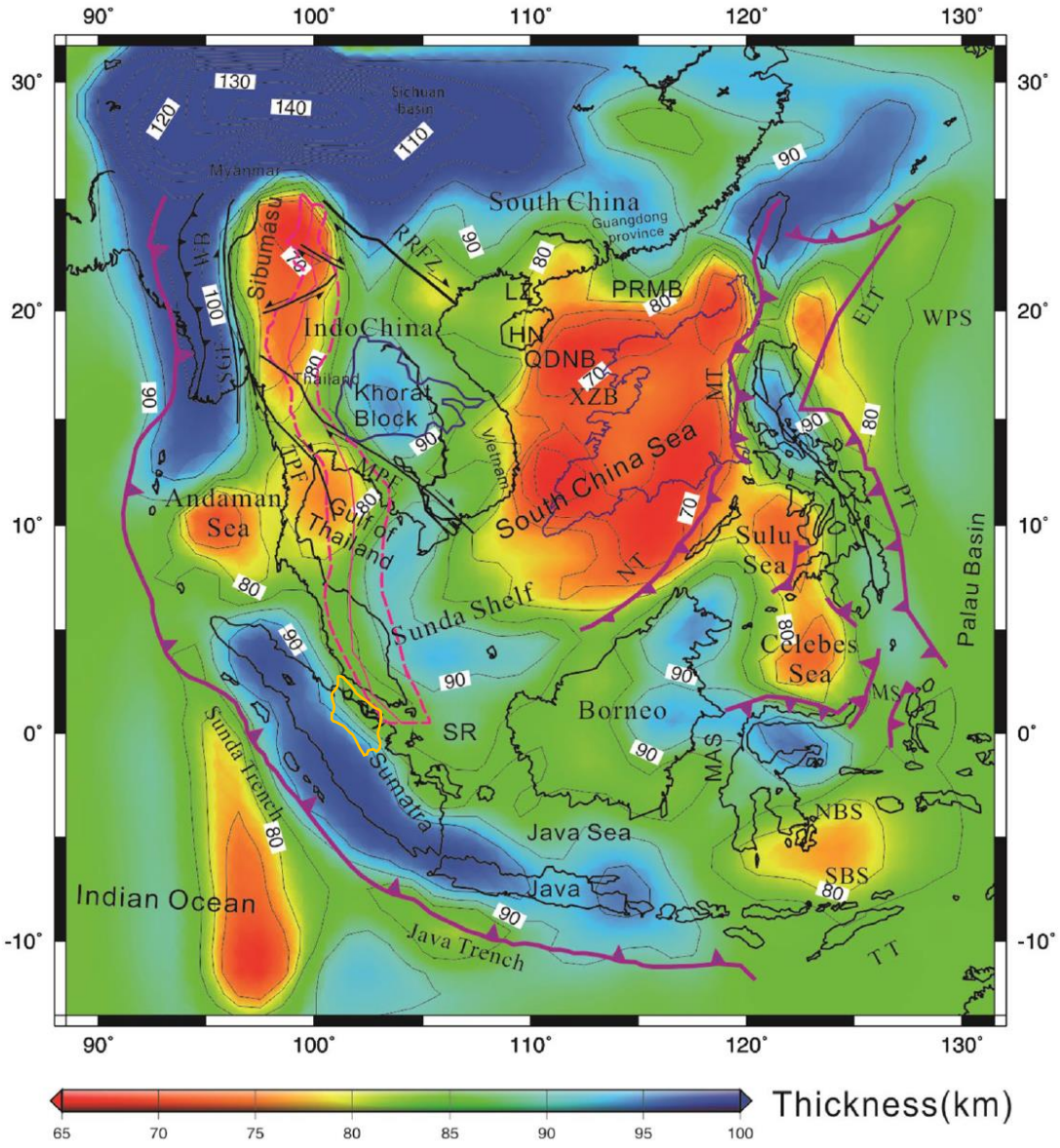

Figure 25. Lithospheric thickness map of Southeast Asia (Yu, et al., 2017), with the Central Sumatra Basin shown in the yellow outline

5.2 Effect of basin structure on the temperature anomaly

On a local scale, the temperature model is also significantly affected by the structure of the Central Sumatra Basin. Figure 26 shows the pattern of localized temperature anomalies at a depth of 2500 m, which coincides with the basement structure of the basin. From the three geological cross-sections, it is evident that the high-temperature anomaly is associated with the basement lows, while the low-

temperature anomaly is associated with the basement highs. At a depth of 2500 m, the temperature map cuts through the basement rock on the basement highs and the Pematang Group which fills the basement lows. This sedimentary unit consists of clastic sediments, including conglomerate, sand, and organic shale, which have lower thermal conductivities than the >500 Ma upper crust granite. Consequently, Pematang Group layer exerts a strongly insulating effect, and it results in the high-temperature anomaly at 2500 m depth, which could be as high as 160°C. On the other hand, the low-temperature anomaly is associated with the basement high, where they were not covered by the Pematang Group. Therefore, the insulating effect does not occur in the area of basement highs, not at 2500 m depth at least.

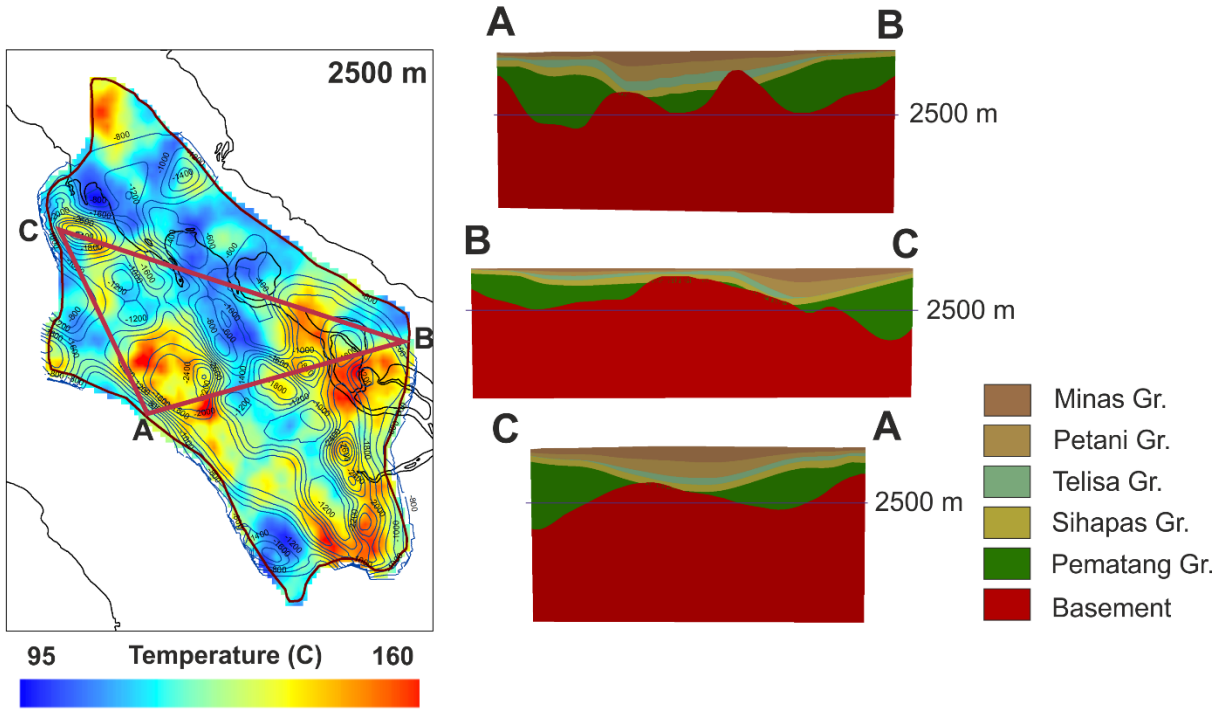

Figure 26. Temperature map from model C4 at a depth of 2500 m, superimposed by the basement contour map (left). Three geological cross-sections from A-B, B-C, and C-A (right)

6 Conclusion

A significantly high-temperature anomaly in the Central Sumatra Basin was suggested by a few researchers, yet it is still poorly constrained. The main objective of this study is to get a better understanding of the thermal characterization in the area. This study requires several steps, including 3D geological modeling and thermal modeling.

The 3D geological model of the sediments and the basement of the area is based on the geological information from 185 wells to build the structural model at the first few kilometers of depth. For this modeling, the geospatial interpolation was performed, which also includes the Triangulated Irregular Network method and the Kernel Smoothing. For the lower part, the structural models were adopted from a global reference model. The structural model includes the sediment layer, upper crust, lower crust, and lithospheric mantle. The sediment layer consists of a few stratigraphic units, namely Pematang, Sihapas, Telisa, Petani, and Minas group.

For the thermal modeling, the temperature measurements from the area were used, which consist of 122 temperature data in total, including 118 uncorrected BHTs and 4 DSTs. Unlike the DST, which has high reliability, the BHT requires correction as the temperature was perturbed during the measurement. The AAPG statistical correction method was used for correcting the BHTs and resulted in BHTx_AAPG with the uncertainties of ±15°C. The average temperature gradient in the area is 52.2 ^{o}C/km, which indicates the high-temperature anomaly in the area. This temperature dataset is used for evaluating the temperature models and also used as an input for advanced data assimilation method to update and improve the temperature models.

The temperature model was initiated by performing multi-1D thermal modeling to populate each grid cell of the model, where the output will be reprocessed for reconstructing the 3D temperature model. The initial prior thermal model from the 3D modeling shows that the model is too cold for representing the observed temperatures in the wells. The sensitivity analysis shows that both the age of the upper-crust granite, which corresponds to the heat production and the lithosphere thickness have huge impacts on the result of the thermal model. According to the model scenario analysis, the model with the best result was obtained by using the lithospheric setting as follow: lithosphere thickness of 90 km and >500 Ma granite for the upper crust.

The temperature anomaly is affected by the lithospheric setting and the basin structure. The relatively thin lithosphere thickness of 90 km partly contributes to a high-temperature anomaly in the area, and it most likely occurs as a response to isostasy, which was triggered by the opening of the Sumatran back-arc basins, including the Central Sumatra Basin. Such geodynamic development is often associated with the Great Sumatran Fault and the Indo-Australian plate subduction towards the Sundaland. The enhanced upper crust heat production post-crustal reworking also contributes to a higher temperature anomaly in the area. The localized pattern of thermal anomalies in the area is also strongly affected by the basin structure, in which the high-temperature anomaly indicates the thermal insulation effect due to a difference in thermal conductivities.

References

Barber, A. J., Crow, M. J. & Milsom, J. S., 2005. *Sumatra. Geology, Resources, and Tectonic Evolution.* IX ed. London: Geological Society Memoir.

Bonté, D. et al., 2010. Subsurface temperature maps in French sedimentary basins: new data compilation and interpolation. *Bulletin de la Société Géologique de France,* Issue 181, pp. 377-390.

Bonté, D., van Wees, J.-D. & Verweij, J. M., 2012. Subsurface temperature of the onshore Netherlands: new temperature dataset and modelling. *Netherlands Journal of Geosciences,* Issue 91, pp. 491-515.

Cameron, N. R., Aspden, J. A., Miswar & Rock, N. M., 1981. *The geology of Tebingtinggi quadrangle, Sumatra (Quadrangle 0719) scale 1:250,000,* Bandung: Geological Survey of Indonesia, Directorate of Mineral Resources, Geological Research, and Development.

Carvalho, H. S. et al., 1980. Terrestrial heat flow in the tertiary basin of Central Sumatra. *Tectonophysics,* pp. 163-188.

Chapman, D., 1986. Thermal gradients in the continental crust. *Geological Society of London Special Publication,* Issue 24, pp. 63-70.

De Coster, G. L., 1974. *The geology of the Central and South Sumatra Basins.* Jakarta, IPA.

Deming, D., 1989. Application of bottom-hole temperature corrections in geothermal studies. *Geothermics,* Issue 18, pp. 775-786.

Doust, H. & Noble, R., 2008. Petroleum systems of Indonesia. *Marine and Petroleum Geology,* Issue 25, p. 103–129.

Emerick, A. & Reynolds, A., 2013. Ensemble smoother with multiple data assimilation. *Computational Geosciences,* Issue 55, pp. 3-15.

Eubank, R. T. & Makki, A. C., 1981. *Structural geology of the Central Sumatra Back-arc Basin.* Jakarta, IPA.

Gard, M., Hasterok, D., Hand, M. & Cox, G., 2019. Variations in continental heat production from 4 Ga to the present: Evidence from geochemical data. *Lithos,* Issue 342-343, pp. 391-406.

Goutorbe, B., Lucazeau, F. & Bonneville, A., 2007. Comparison of several BHT correction methods: a case study on an Australian dataset. *Geophysical Journal International,* Issue 170, pp. 913-922.

Grysen, T., Gibson, D. & Nicholson, K., 2016. *Geothermal (heat flow) map of the Sumatra,* Munchie: 50th Annual GSA North-Central Section Meeting.

Guo, W. & Langevin, C., 2002. *User's Guide to SEAWAT: A Computer Program for Simulation of Three-Dimensional Variable-Density Ground-Water Flow,* Reston: U.S. Geological Survey.

Hall, R., 2002. Cenozoic geological and plate tectonic evolution of SE Asia and the SW Pacific: Computer-based reconstructions, model and animations. *Journal of Asian Earth Sciences,* pp. 353-431.

Hall, R. & Spakman, W., 2015. Mantle structure and tectonic history of SE Asia. *Tectonophysics,* Issue 68, p. 14–45.

Hantschel, T. & Kauerauf, A., 2009. *Fundamentals of Basin and Petroleum Systems Modelling.* ISBN-978-3540723172 ed. Heidelberg: Springer Berlin.

Harrison, W. E., Luza, K. V., Prater, M. L. & Chueng, P. K., 1983. Geothermal resource assessment of Oklahoma. *Oklahoma Geological Survey, Special Publication,* 81(1), pp. 1-42.

Hasterok, D. & Chapman, D., 2011. Heat production and geotherms for the continental lithosphere. *Earth and Planetary Science Letters,* Issue 307, pp. 59-70.

Heidrick, T. L. & Aulia, K., 1993. *A structural and tectonic model of the coastal plains block, Central Sumatra Basin, Indonesia.* Jakarta, IPA 22nd Annual Convention Proceedings.

Hofmeister, A., 1999. Mantle values of thermal conductivity and the geotherm from phonon lifetimes. *Science,* Issue 283, pp. 1699-1702.

Hutchison, C. S., 1994. Gondwana and Cathaysian blocks, Palaeotethys sutures and Cenozoic tectonics in South-East Asia. *Geologische Rundschau,* Issue 82, pp. 388-405.

Jones, C. R., 1961. *A revision of the stratigraphical sequence of the Langkawi Islands, Federation of Malaya.* Bangkok, Proceedings of the 9th Pacific Congress.

Laske, G., Masters, G., Ma, Z. & Pasyanos, M., 2013. *Update on CRUST1.0 - A 1-degree Global Model of Earth's Crust.* San Diego, EGU.

Li, J. & Heap, A. D., 2014. Spatial interpolation methods applied in the environmental sciences: A review. *Environmental Modelling & Software,* Issue 53, pp. 173-189.

Limberger, J. et al., 2017a. A public domain model for 1D temperature and rheology construction in basement-sedimentary geothermal exploration: an application to the Spanish Central System and adjacent basins. *Acta Geodaetica et Geophysica,* Issue 52, pp. 269-282.

Luijendijk, E. et al., 2011. Thermal state of the Roer Valley Graben, part of the European Cenozoic Rift System. *Basin Research,* Issue 1, pp. 65-82.

McKenzie, D. & Priestley, K., 2008. The influence of lithospheric thickness variations on continental evolution. *Lithos,* 102(1-2), pp. 1-11.

Mertosono, S. & Nayoan, G. A., 1974. *The Tertiary basinal area of Central Sumatra.* Jakarta, IPA.

Metcalfe, I., 1996. Pre-Cretaceous evolution of SE Asian terranes. In: R. Hall & D. J. Blundell, eds. *Tectonic evolution of Southeast Asia.* London: Geological Society, pp. 97-122.

Mitas, L. & Mitasova, H., 2001. Spatial Interpolation. *Geographical information systems: principles, techniques, management and applications,* I(2), pp. 481-492.

Nawawi, A. et al., 1996. Petroleum Geology of Indonesian Basins: Central Sumatra Basins. In: *Petroleum Geology of Indonesian Basins: Principles, Methods, and Application.* Jakarta: Pertamina BPPKA (Foreign Contractors Ventures Development Body).

Pubellier, M. & Morley, C. K., 2014. The basins of Sundaland (SE Asia): Evolution and boundary conditions. *Marine and Petroleum Geology,* Volume 58, pp. 555-578.

Rogers, J. W., 1996. A History of Continents in the Past Three Billion Years. *The Journal of Geology,* 104(1), pp. 91-107.

Rychert, C. A. & Shearer, P. M., 2009. A Global View of the Lithosphere-Asthenosphere Boundary. *Science,* 324(5926), pp. 495-498.

Schatz, J. & Simmons, G., 1972. Thermal conductivity of Earth materials at high temperatures. *Journal of Geophysical Research,* Issue 77, pp. 6966-6983.

Sekiguchi, K., 1984. A method for determining terrestrial heat flow in oil basinal areas. *Tectonophysics,* Issue 103, pp. 67-79.

Tapponier, P. et al., 1982. Propagating extrusion tectonics in Asia: new insights from simple experiments with plasticine. *Geology,* Issue 10, pp. 611-616.

Wand, M. P. & Jones, M. C., 1995. *Kernel Smoothing.* 1st ed. New York: Chapman & Hall.

Webster, R. & Oliver, M., 2001. *Geostatistics for Environmental Scientists.* Chichester: John Wiley & Sons, Ltd.

Workman, R. & Hart, S., 2005. Major and trace element composition of the depleted MORB. *Earth Planet. Sci. Lett.,* Issue 231, pp. 53-72.

Xu, Y. et al., 2004. Thermal diffusivity and conductivity of olivine, wadsleyite, and ringwoodite to 20 GPa and 1373 K. *Physics of the Earth and Planetary Interiors,* pp. 143-144, 321-336.

Yu, C. et al., 2017. Deep thermal structure of Southeast Asia constrained by S-velocity data. *Mar Geophys Res,* Issue 38, pp. 341-355.

Zahirovic, S., Seton, M. & Müller, R. D., 2014. The Cretaceous and Cenozoic tectonic evolution of Southeast Asia. *Solid Earth,* Issue 5, pp. 227-273.

Appendix

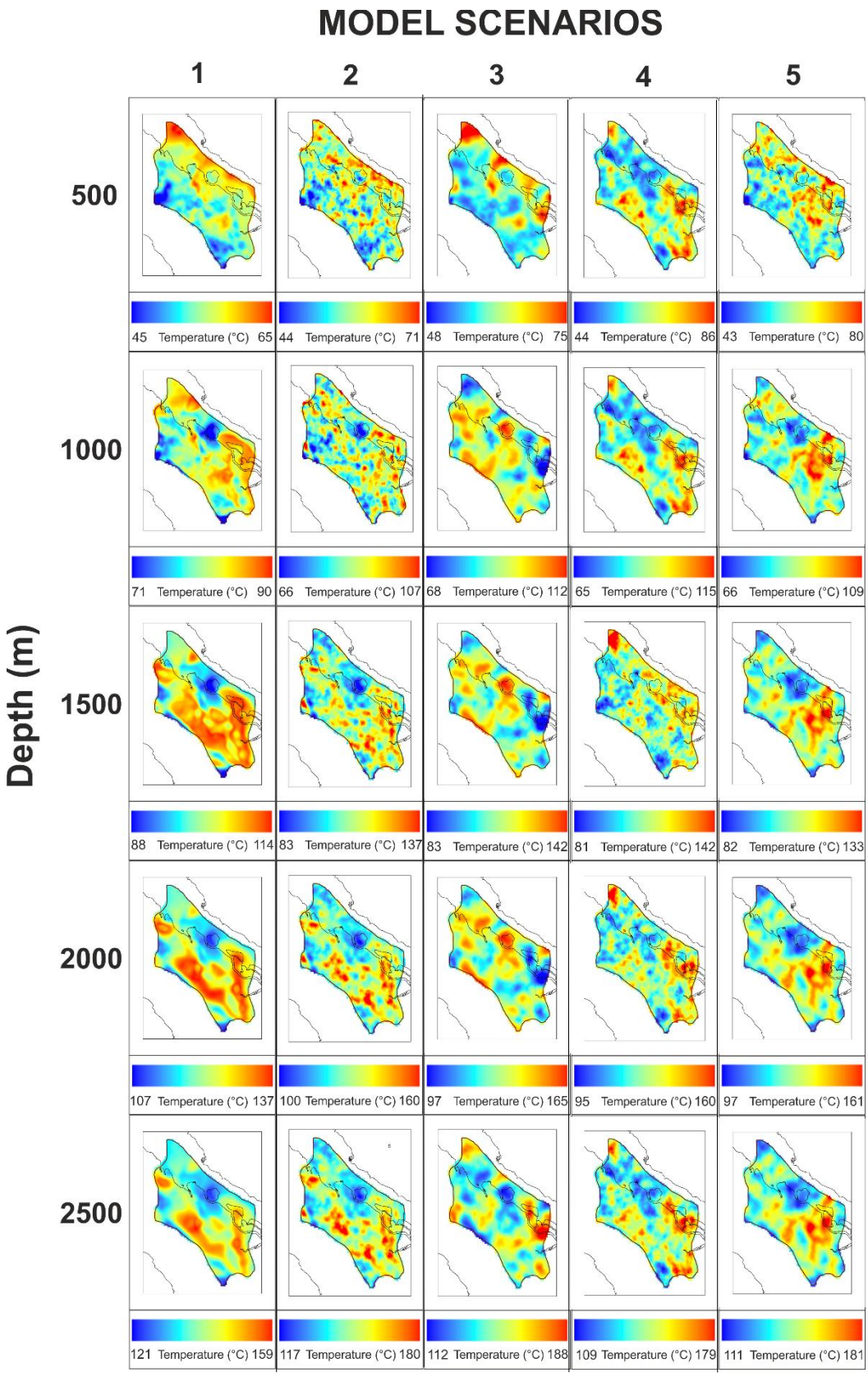
MODEL SCENARIOS
1
2
3
4
5
Depth (m)
500
1000
1500
2000
2500
45 Temperature (°C) 65
44 Temperature (°C) 71
48 Temperature (°C) 75
44 Temperature (°C) 86
43 Temperature (°C) 80
71 Temperature (°C) 90
66 Temperature (°C) 107
68 Temperature (°C) 112
65 Temperature (°C) 115
66 Temperature (°C) 109
88 Temperature (°C) 114
83 Temperature (°C) 137
83 Temperature (°C) 142
81 Temperature (°C) 142
82 Temperature (°C) 133
107 Temperature (°C) 137
100 Temperature (°C) 160
97 Temperature (°C) 165
95 Temperature (°C) 160
97 Temperature (°C) 161
121 Temperature (°C) 159
117 Temperature (°C) 180
112 Temperature (°C) 188
109 Temperature (°C) 179
111 Temperature (°C) 181